Plenoptic BOS: Combining a Plenoptic Camera with the Background Oriented Schlieren Technique

by

Jenna Nicole Klemkowsky

A thesis submitted to the Graduate Faculty of
Auburn University
in partial fulfillment of the
requirements for the Degree of
Master of Science

Auburn, Alabama
December 10, 2016

Keywords: schlieren, background oriented schlieren, plenoptic camera, light field imaging

Approved by

Brian S. Thurow, Chair, Associate Professor of Aerospace Engineering
Stanley J. Reeves, Professor of Electrical and Computer Engineering
David E. Scarborough, Professor of Aerospace Engineering

Abstract

The background oriented schlieren (BOS) technique is a method of observing the refraction of light rays passing through a density varying medium. When used with a conventional imaging system, this technique captures a single line-of-sight integrated quantity that is a result of the refractive index gradients associated with the density varying medium. With the inherent three-dimensionality of most flow fields, an alternative imaging system called the plenoptic camera has been introduced to the scientific community as a viable option in 3D BOS systems. This camera has the ability to capture 3D information in a single snapshot, which allows for images of different perspectives and different focal planes to be generated from a single raw plenoptic image. The integration of a plenoptic camera into the BOS technique, termed plenoptic BOS, is discussed in this work. The use of a plenoptic camera in a BOS setup provides the ability to acquire multiple line-of-sight integrated quantities, which can be used to create a BOS light field similar to that of the original light field captured by the plenoptic camera. This type of structured BOS light field allows for the ability to computationally generate focused schlieren images through the volume. The experiments used to explore this new technique include an arrangement with two flames placed at different depths and a setup of a single heated jet placed at ten different locations within the field of view. The former arrangement provided the ability to qualitatively highlight gradients being produced at different depths in 3D space. The latter arrangement explored the sensitivity of the BOS setup with respect to the jet's position relative to the background as well as the ability to quantify the jet's position in 3D space based on the collected measurements. Such results provide motivation to further explore the plenoptic BOS technique, improve the algorithms associated with depth estimation, and ultimately progress towards a truly 3D reconstruction of a density field.

Acknowledgments

There are so many people that have supported and encouraged me during this educational endeavor, and I would not be where I am today if it weren't for them. I would first like to thank my advisor, Dr. Thurow, for his advice and assistance during the development of this research. His passion for research is contagious, his commitment to his students is unending, and his patience with me is very much appreciated as I encounter obstacles along this journey. I would also like to thank Dr. Reeves and Dr. Scarborough for taking the time to be on my committee and for providing valuable conversations during my graduate school journey thus far. I also express gratitude to the Advanced Flow Diagnostics Laboratory. I appreciate their willingness to work collaboratively as well as their humor, friendship, and support.

I would also like to thank my parents, Tammy and Pete Klemkowsky for encouraging me to pursue my passions. They have always supported any decision I've made, even if it meant moving far from home to further my education. I also truly appreciate the support of my sister, Ashley Klemkowsky, as well as Cameron Johnson and Matthew Malone for their unending reassurance and praise during the course of this work. The unconditional love I've received from these people as well as so many friends and family members has been a reminder that no success is considered valuable unless you are able to share it with others. I am blessed to be surrounded by such wonderful people on a daily basis, and I will forever be grateful for their guidance.

Table of Contents

Abstract ii

Acknowledgments iii

List of Figures vi

List of Tables xii

List of Abbreviations xiii

1 Introduction 1

2 Review of Schlieren Techniques 5

2.1 Conventional Schlieren 5

2.2 Shadowgraphy 10

2.3 Background Oriented Schlieren 11

2.4 Focused Schlieren 17

2.5 Summary of Schlieren Techniques 19

3 3D Measurements Using Schlieren Techniques 20

3.1 3D Measurements with a Single Camera BOS System 21

3.2 3D Measurements with a Multi-Camera BOS System 24

3.3 3D Measurements with a Light Field Probe 26

3.4 3D Measurements with a Single Plenoptic Camera BOS System 28

3.5 Summary of 3D BOS Methods 29

4 Light Field Imaging and a Plenoptic Camera 31

4.1 History of the Plenoptic Function and the 4D Light Field 31

4.2 The Plenoptic Camera and Its' Capabilities 32

5 Depth of Field 40

6 Background Oriented Schlieren with a Plenoptic Camera: Plenoptic BOS 43

6.1 Basic Concept 43
6.2 Generation of the BOS Light Field 43
6.3 BOS Refocusing 45
7 Experimental Arrangements 48
7.1 Experiment One: Two Flame Sources 49
7.2 Experiment Two: A Single Heated Jet 50
8 Post Processing and Discussion of Results 54
8.1 Experiment One: Two Flame Sources 54
8.2 Experiment Two: A Single Heated Jet 59
9 Conclusions and Future Work 65
Bibliography 68

List of Figures

2.1 Schematic of a conventional schlieren arrangement using a point light source and two lenses. Adapted from Settles [13]. 7

2.2 Schematic of a conventional schlieren arrangement using a point light source and two parabolic mirrors. Adapted from Settles [13]. 8

2.3 Examples of the use of the schlieren technique towards a wide variety of applications. 9

2.4 Schematic of a shadowgraphy setup using a point light source, a lens, and a viewing screen to project the light onto. 11

2.5 A Blue Angel F/A-18 Hornet [1] distorting the background during flight shows the same concept that the BOS technique exploits during an experiment. 12

2.6 Experimental schematic of the BOS technique, where the camera is represented by a simple lens and image sensor. The disturbance is assumed to occur at an infinitesimally thin plane without any other disturbances occurring between the background and the camera. Adapted from Bichal [9]. 13

2.7 A schematic of the geometric relationships observed in a BOS configuration, where the displacement observed on the image sensor, d_i, can be traced back to an apparent shift in the background in physical space. The angle, ε, is used to calculate this shift in physical space based on known parameters for an experiment. Adapted from Bichal [9]. 14

2.8 Examples of the BOS technique used towards a wide variety of applications. . . 16

2.9 Schematic of a focused schlieren system with an extended light source channeling the light through a source grid and cutoff grid onto the image plane. Adapted from Goulding [17]. 17

2.10 Results from an experiment performed by Floryan *et al.* [2] using two jets placed 13 millimeters apart. 18

3.1 Examples of the common setups used to obtain 3D information. (a) Rotating the schlieren object has been performed by Cabaleiro *et al.* [3] (b) A multi camera configuration has been used by Atcheson *et al.* [4]. 20

3.2 The density distribution of an under-expanded free jet of air using a double hole orifice reported by the work of Goldhahn *et al.* [5], where (a) is a slice along the jet axis and both (b) and (c) are different slices in the z-plane. 22

3.3 Results of an asymmetric model placed in a supersonic wind tunnel reported by the work of Ota *et al.* [6]. A single slice of the density distribution is shown along central plane of the asymmetric body on the left, and the 3D density distribution is shown alongside surfaces possessing constant density on the right. 23

3.4 Volumetric time-resolved results reported by the work of Atcheson *et al.* [4] of a hot air plume above a gas burner. 25

3.5 Results reported by the work of Nicolas *et al.* [7] The left image shows a 3D density reconstruction, the center image shows a (y, z) plane slice, and the right image shows a (x, y) plane slice of the plume of a candle. 26

3.6 Results reported by the work of Wetzstein *et al.* [8], where a spatio-angular filter helped to determine the vertical ray displacement and the horizontal and vertical refractive index gradients per-pixel. 27

3.7 Results reported by the work of Bichal [9] showing a visual comparison of the density distribution determined from simulated data (left) and experimental data (right) for a single slice within the volume. 29

4.1 (a) Schematic of the 5D parameterization of the light field in terms of three spatial coordinates and two angular coordinates. (b) The redundancy of one spatial coordinate is eliminated based on the assumption that nothing is occluding the light ray's path. This schematic shows the 4D parameterization of the light field as it intersects with two planes: (u, v) and (s, t). Both schematics adapted from Levoy [10]. 33

4.2 Schematic of the components that make up a plenoptic camera. Light rays emanating from a point source at the focal plane with pass through the main lens, through a specific microlens, and depending on their angle, project onto different pixels on the image sensor. 34

4.3 (a) A schematic showing how a specific portion of the main lens corresponds to a single pixel behind each microlens that that used to render a perspective image. Adapted from Ng *et al.* [11]. (b) A plenoptic camera consisting of only 4 microlenses in the array generates a single output perspective image by choosing the same pixel location from behind each of the 4 microlenses. 35

4.4 An example of a raw plenoptic image, where aliasing is present due to the downsampling of a 29MP image to fit the format of this document. A zoomed in portion of the image is shown on the right, where individual microlenses are observed. 36

4.5 Examples of rendered perspective view images. A leftmost perspective view is shown on the left and a rightmost perspective view is shown on the right. 37

4.6 Schematic of the ability to synthetically change the focal plane from the original nominal focal plane in the raw plenoptic image. The new synthetic film plane is represented by $\alpha\ s_i$, where α defines the relative depth of the new plane with respect to the original plane. 38

4.7 Examples of two refocused images rendered by using $\alpha = 1.15$ on the left to synthetically place the focal plane closer in the scene and by using the nominal focal plane with $\alpha = 1$ on the right. 39

5.1 Relationship between object distance and the DOF for three different lenses. . . 41

6.1 Schematic representing a simplified version of generating the BOS light field, where three perspective view image pairs are used. The vector shown in the top center portion of each perspective view represents a 2×2 region of microlenses in the array. For each of the four microlenses, the vector value for each perspective view corresponds to the same pixel location behind each microlens. 46

7.1 Side view schematic of the Plenoptic BOS setup observing two flames produced at different depths within the scene. 51

7.2 Schematic of the experimental BOS setup of a single heated jet performed at the NASA Langley Research Center. The region of interest is the portion of the DOF used during these experiments, where the heated jet was placed at ten different positions within this region. 52

8.1 Overlaid image of the cropped region of vectors determined from cross-correlation of the center perspective image pair on top of center perspective of the two flames themselves. This provides visual guidance as to the location of the two flames within the setup. 54

8.2 Examples of the magnitude of the displacement vectors obtained from the cross-correlation of three different perspectives view image pairs. Each sub-image contains 116×86 displacement vectors. 56

8.3 Refocused BOS images where the magnitude of the distortions of the front and back flame are in-focus at different depth positions. 57

8.4 Comparison of the results produced by a single focused BOS image and a single perspective view cross-correlation. 58

8.5 Refocused BOS images where the x-displacement of the distortions of the front and back flame are in-focus at different depth positions. 58

8.6 Refocused BOS images where the y-displacement of the distortions of the front and back flame are in-focus at different depth positions. 59

8.7 Results of plenoptic BOS using an average of the 25 heated jet images versus using an instantaneous heated jet image. Both images have been rendered for the focal plane position corresponding to their depth position of 762 mm in front of the nominal focal plane. 60

8.8 Error of the depth estimation method versus the actual position of the jet measured with respect to the distance away from camera in terms of millimeters. The near and far DOF limits are also shown for each jet position, and a horizontal error bar represents the finite width of the jet being imaged. 61

8.9 Maximum gradient values per slice of each of the 500 slices in the focal stack of focused BOS images generated for each of the ten different jet positions. The maximum gradients are plotted with respect to the distance from the camera in millimeters. 63

8.10 Maximum gradient values per slice of each of the 500 slices in the focal stack of focused BOS images generated for (a) the front most jet position and (b) the back most jet position. 64

List of Tables

7.1 Computational time for each step in the plenoptic BOS process. 49

List of Abbreviations

μm	micrometers
ρ	density
ε	angular ray deflection
c_o	Circle of confusion in object space
d_a	Diameter of the main lens aperture
d_i	Displacement of background in image space
d_o	Displacement of background in object space
d_{eff}	Effective diameter of the aperture used to generate a perspective view
f_{micro}	Focal length of the microlenses
$G(\lambda)$	Gladstone-Dale constant
p_p	Pixel pitch
s_i	Distance in image space according to the thin lens equation
s_i'	Distance in image space to the synthetic film plane
s_o	Disatnce in object space according to the thin lens equation
s_o'	Distance in object space to the synthetic film plane
s_{far}	Far depth of field limit
s_{near}	Near depth of field limit

α	Scalar value used to calculate relative depth of s_i' to s_i
λ	Any wavelength of light
2D	Two-Dimensional
3D	Three-Dimensional
3DDMT	3D Density Measurement Technique
4D	Four-Dimensional
5D	Five-Dimensional
AFDL	Advanced Flow Diagnostics Laboratory
ART	Algebraic Reconstruction Technique
B	Distance from the schlieren object plane to the background
BOS	Background Oriented Schlieren
DOF	Depth of Field
f	focal length of the main lens
FBP	Filtered Back Projection
L	Distance from the main lens to the schlieren object plane
LFIT	Light Field Imaging Toolkit
LICT	Laser Interferometric Computed Tomography
MART	Multiplicative Algebraic Reconstruction Technique
mm	millimeter
n	index of refraction

PIV Particle Image Velocimetry

SNR Signal-to-Noise Ratio

Chapter 1

Introduction

Schlieren-based flow visualization techniques represent a classical method of observing optical inhomogeneities by exploiting the refraction of light passing through a density varying flow field [12]. The direct relationship between light's refraction and variations in density provides the ability to integrate along the line-of-sight of an imaging system in order produce two-dimensional (2D) qualitative images of the inhomogeneous density field. The origins of the conventional schlieren technique dates back to the 1600s through John Locke's observation of refractive index change due to convection of a lit candle, though the scientific community was not fully aware of such a technique until the contributions made by Foucault and Toepler in the 19th century [12]. Both scientists acted as major catalysts in the optical exploration of inhomogeneous media, and since its introduction to the scientific community, these techniques have provided successful qualitative results towards a wide range of transparent media visualization applications.

Since the original development of conventional schlieren, variations of this technique have been added to the group of schlieren-based techniques. This includes shadowgraphy [13, 14], the background oriented schlieren technique (BOS) [15, 16, 14], and the focused schlieren technique [17, 2]. Each setup has proven to be sensitive to small changes in density and is often favorable in a scientific setting because they are non-intrusive in nature. The BOS technique is known for its' simple configuration with few material requirements. The concept of BOS was first purposed in a patent filed by Meier in 1999 [15]. This technique acquires images of a randomly textured background pattern with and without the density disturbance between the imaging system and the background. In the post-processing period, the images are compared to observe the apparent shift in the background pattern due to the

refraction of the light rays. The use of this technique with a conventional camera provides a single 2D line-of-sight integrated quantity represented by displacement vectors obtained during image comparison.

While 2D qualitative images provide the ability to observe media that cannot be seen with the human eye, most flows are inherently three-dimensional (3D). This reality motivates the advancement of schlieren-based techniques towards both 3D and quantitative measurements. Most current 3D schlieren approaches require the acquisition of views from different relative angles. Such views can be acquired either using multiple cameras or rotating the object producing the density variations. With BOS being the focus of the current work, there are several researchers that have used multi-camera configurations to obtain BOS measurements including the work of Atcheson *et al.* [18], who used a 16 camera configuration to produce the first volumetric, time-resolved BOS imaging system of a plume above a flame. More recently, a 12 camera configuration was implemented by Nicolas *et al.* to reconstruct the density field of an underexpanded jet [19]. The implementation of several projection angles using a single camera has also been used in a BOS setup such as the work of Ota *et al.* [20] who used a single camera to explore an axisymmetric jet in a supersonic wind tunnel by capturing 19 different projection angles of a color grid background made up of horizontal and vertical stripes. Using 36 projections, Goldhahn and Seume [5] were able to reconstruct the 3D density field of an underexpanded free jet of air out of a double hole orifice. These experimental setups are just some of the many that have deemed success in 3D schlieren experiments, but these type of complex configurations are not always desirable, especially in facilities with limited optical access.

The technological development of a plenoptic camera [21, 22, 11, 23] expands upon the idea of what it means to capture an image. A plenoptic camera provides a new way to capture the total light ray distribution of a scene, or light field, in terms of spatial and angular coordinates. The uniqueness of this camera configuration lies in the addition of a microlens array placed in between the main lens and the image sensor. This addition

provides the capability to render images from different perspectives and with different focal planes, each of which is performed in the post-processing period. The ability to acquire 3D information in a single snapshot with a single camera provides the potential to implement this technology with regards to schlieren-based techniques.

The objective of the current work is to explore the integration of a plenoptic camera into a conventional BOS measurement system in order to obtain 3D, qualitative density gradient measurements and use such information to estimate the depth location of density gradients. The resulting technique, termed plenoptic BOS, produces images similar to that of a conventional BOS experiment. Unlike conventional BOS, however, this novel technique extends the capability to allow for changes in perspective (i.e. changes in the line-of-sight) within a single image as well as the ability to generate 'focused BOS' images. These are characterized by a relatively narrow depth-of-field in comparison with traditional BOS images. These focused BOS images highlight density gradients at a particular synthetic focal plane in contrast to gradients that are out of focus. With the ability to exploit flow field information acquired beyond the capabilities of a conventional camera, the purpose of this current work is to feature a step-by-step explanation of how this single plenoptic camera, non-intrusive technique works. Such a process provides the ability to use qualitative density gradient information to preliminarily assign quantitative depth to a sharp density gradient at a well-defined location in 3D space.

Chapters II and III provide the background information on schlieren techniques and the 3D experimental successes of these techniques. These chapters are designed to review what has been done before as well as provide motivation for the current work. Chapter IV provides the foundation of light field imaging, the plenoptic camera, and the mathematical equations that highlight the capabilities of a plenoptic camera. With the foundation of both schlieren techniques and plenoptic imaging laid, Chapter V stresses the importance of how depth of field influences both the BOS and plenoptic imaging systems separately. This chapter provides the importance of understanding both items individually before merging

them together in Chapter VI, where the idea of plenoptic BOS is introduced. This chapter is designed to walk the reader through the steps required to achieve successful plenoptic BOS results. This includes the post-processing steps that combine both the demands of BOS and plenoptic imaging to be able to interpret the acquired data set.

Chapters VII and VIII discuss the set up and analysis of two proof of concept experiments that are used to show the feasibility of this new visualization technique. The first experiment explores two flames placed at different depth locations within a scene. This experiment exploited the refocusing capability of a plenoptic camera in order to qualitatively highlight density gradients being produced at different depths. The second experiment used a single hot-aired jet within the scene. The jet was placed at ten different locations in front of or behind the nominal focal plane, which explored two concepts: 1) how the sensitivity of the setup changed with respect to the jet's position from the nominal focal plane, and 2) how well the spatial location was quantified based on the sharpness of the density gradient at a known position in 3D space. Both experiments convey the practicality of this technique in order to both qualitatively and quantitatively explore the three dimensionality of a flow field with the use of a single camera. These results provide reason to further explore this new technique, especially with its potential to simplify an approach in limited optical access facilities, where there is desire to estimate depth and obtain 3D density measurements.

Chapter 2

Review of Schlieren Techniques

The following chapter lays the foundation of the basis of the conventional schlieren technique as well as a discussion of some of the schlieren technique variations including: shadowgraphy, background oriented schlieren, and focused schlieren. Each of these techniques has been used to observe the density gradients present in a flow field qualitatively and/or quantitatively. While there are other techniques that explore the density features within a flow field, the focus of this section is to inform the reader about the relevant schlieren techniques that have been explored during the course of this research.

2.1 Conventional Schlieren

In the 17^{th} century, Robert Hooke made several scientific discoveries including the discussion of light's refraction created by density variations in his work *Micrographia* [24]. In this work, he discussed the relevance of this phenomena towards both gases and liquids including: the twinkling of stars and the convection of fluids [13]. The understood relationship between refractive index and density is known today as the Gladstone Dale equation shown in Equation 2.1, where ρ represents the density, n represents the refractive index, and $G(\lambda)$ is a constant for a specific gas. Though Hooke was able to observe this relation through the shadows of a convective plume, his work in this field of study was not really shared with the public or explored further until centuries later [13].

$$\frac{n-1}{\rho} = G(\lambda) \tag{2.1}$$

In the 19th century, both J. B. Leon Foucault and August Toepler each observed certain phenomenon similar to Hooke's observations. Foucault exploited this concept to improve the mirrors in telescopes while Toepler explored this concept during his doctoral studies [13]. During this time, Toepler named this imaging technique the *schlieren* technique, and he was the first to develop a practical apparatus used in a schlieren-based configuration. This configuration as well as many variations of this configuration are still used today. A conventional schlieren setup is shown in Figure 2.1, where the system uses two lenses and a point light source. The light beam emanating from the point light source is collimated by $L1$ before it passes through the test area. If a disturbance is not present in the test area, the light will remain on the collimated path until passing through the second lens, $L2$. Upon passing through $L2$, the light will converge to a single point before re-spreading onto the image sensor. At the location in which the light converges to the smallest point, a knife edge is placed to cut off 50% of the light. If a disturbance is present within the test area, the light will refract upon passing through the disturbance following the blue dotted line in Figure 2.1. As this refracted light beam passes through $L2$, the light ray will either be cut off by the knife edge (like the blue dotted line) or pass above the knife edge. This results in either a dark or light spot on the image sensor respectively. In this particular example the knife edge has a horizontal orientation, therefore it is observing the light rays refracting vertically. The knife edge can also be placed vertically, which will provide observations of light rays refracting is the horizontal direction.

The inhomogeneities in the the medium refract the light rays in proportion to the gradients of refractive index in the (x, y) plane. This is assuming the the light rays are traveling along the z-axis and refract vertically and horizontally according to this (x, y, z) coordinate system. Equations 2.2 and 2.3 represent the curvature of the light rays mathematically. Both of these equations show that the curvature of a refracted light ray is related to the magnitude of the refractive-index gradient [14].

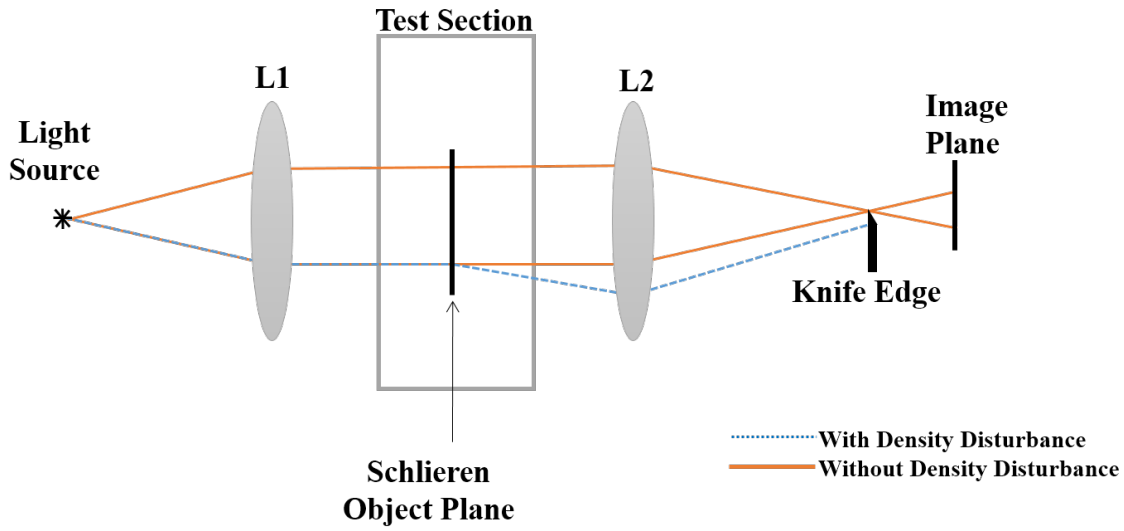

Figure 2.1: Schematic of a conventional schlieren arrangement using a point light source and two lenses. Adapted from Settles [13].

$$\frac{\partial^2 x}{\partial z^2} = \frac{1}{n}\frac{\partial n}{\partial x} \tag{2.2}$$

$$\frac{\partial^2 y}{\partial z^2} = \frac{1}{n}\frac{\partial n}{\partial y} \tag{2.3}$$

The results of a schlieren image (i.e. the angular ray deflection) are performed by integrating along the line-of-sight with regards to their respective directional component. The mathematical expressions for x and y angular deflections (ε) are shown in Equations 2.4 and 2.5. These expressions show that the deflections observed using this technique are related to the gradient of the refractive index rather than the refractive index value itself. As noted in Settles *et al.* [13], these expressions also show that the light rays tend to refract towards regions of higher refractive index and thus refract towards regions of higher density.

$$\varepsilon_x = \frac{1}{n}\int \frac{\partial n}{\partial x}\partial z \tag{2.4}$$

$$\varepsilon_y = \frac{1}{n} \int \frac{\partial n}{\partial y} \partial z \tag{2.5}$$

There are several variations to the conventional schlieren setup. One of the most common variations includes the use of two spherical, parabolic mirrors instead of the use of two lenses to channel the light appropriately. A schematic of this Z-type setup is show in Figure 2.2, whose name comes for the noted 'Z' formation of all components [13]. This figure is similar to that of Figure 2.1, where the undisturbed lights rays are represented by the orange lines and a light ray passing through a density disturbance is represented by the blue dotted line. Terms $M1$ and $M2$ represent the two mirrors used to collimate the light and then focus the light back down such that the beam passes the knife-edge (or is potentially cut-off by the knife edge) and lands on the image sensor of the imaging system. Just like the use of lenses, the use of mirrors observes the first spatial derivative of the refractive index.

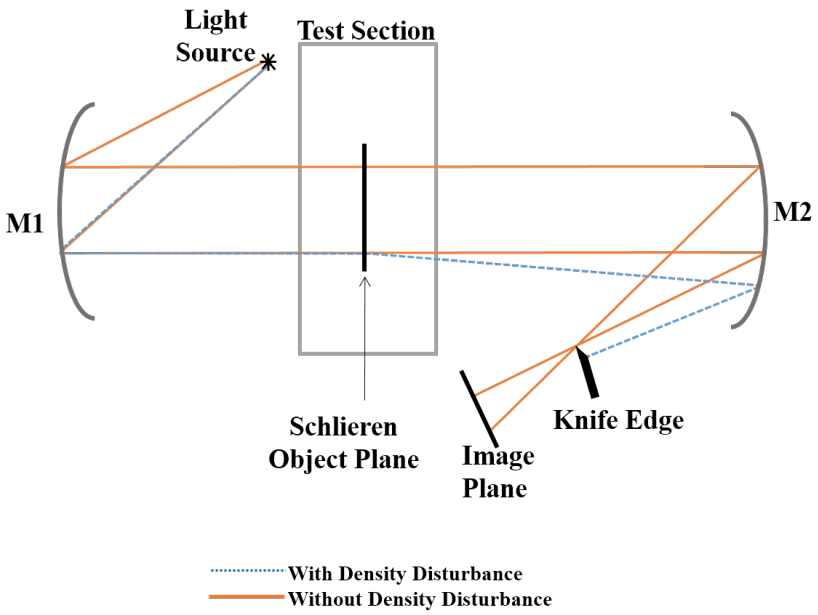

Figure 2.2: Schematic of a conventional schlieren arrangement using a point light source and two parabolic mirrors. Adapted from Settles [13].

Conventional schlieren has been used towards a wide range of applications. These applications include some of those shown in Figure 2.3 such as a bullet fired from a gun

[25], the thermal plume from a candle [26], the heat rising off a hot cup of coffee [27], and the shock waves produced by a test object in the wind tunnel facility [28]. These examples, though just a few of the many times schlieren imaging has been used, show the versatility of this technique in qualitatively observing the density gradients present in a flow field.

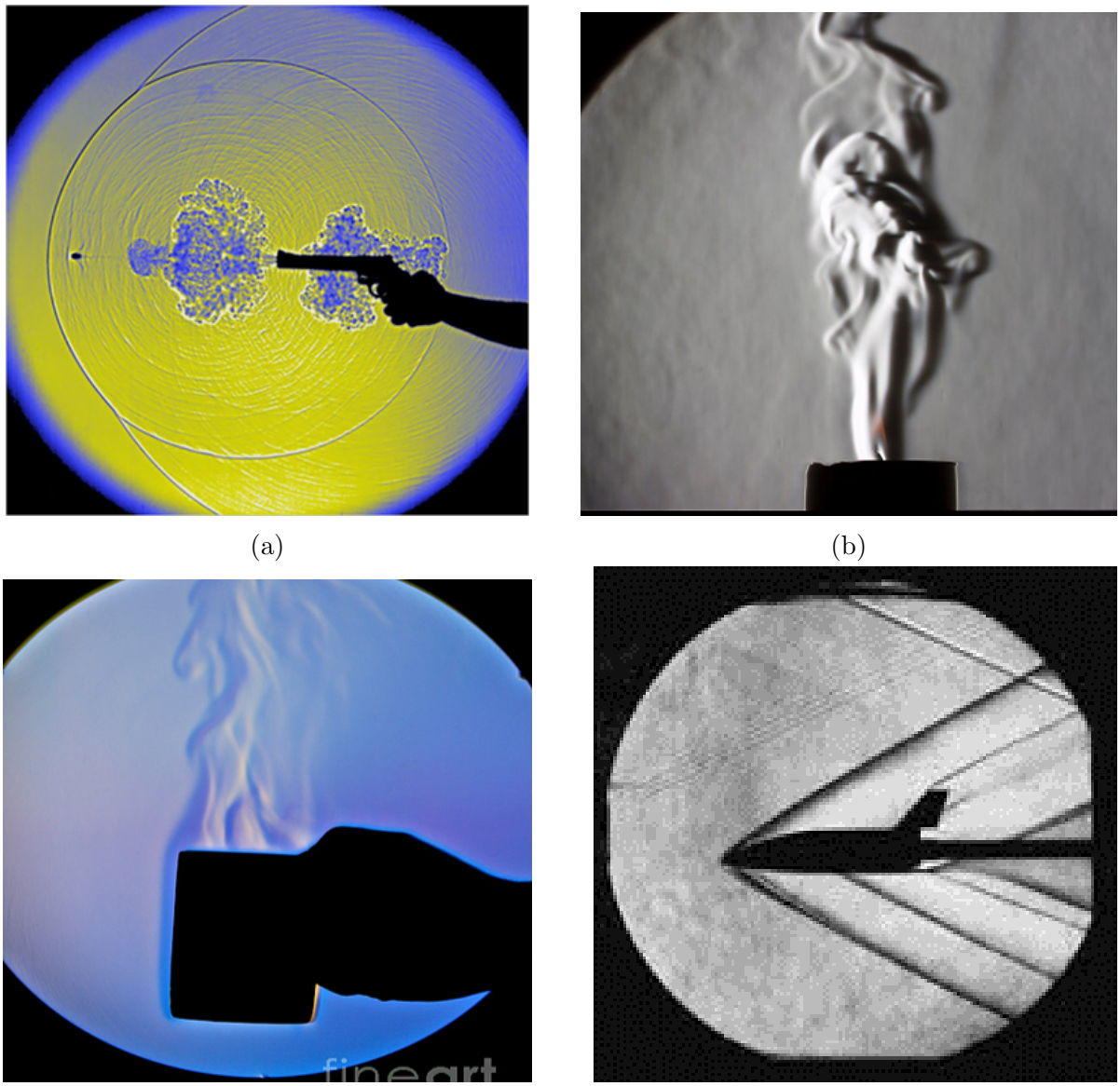

(a) (b)

(c) (d)

Figure 2.3: Examples of the use of the schlieren technique towards a wide variety of applications.

2.2 Shadowgraphy

A much simpler form of the conventional schlieren technique is known as shadowgraphy, which does not require the use of a knife edge. As the name states, the results of this type of setup result in a shadow being cast by the schlieren object. A schematic of a typical setup is shown in Figure 2.4, where only a light source, a lens, the schlieren object, and a viewing screen are required. The viewing plane is a representation of an image sensor, a white piece of paper, a wall, or the like.

Light traveling from the light source (noted here as a point source) will be collimated after passing through $L1$ and will evenly illuminate the viewing screen without the presence of the schlieren object. This is represented as if the light rays were following the orange lines in Figure 2.4. When the schlieren object is placed between the screen and the light source, light rays passing through the schlieren object will refract from its original path just like conventional schlieren. Rather than a knife edge cutting off half the light, the viewing screen will observe a decrease in illumination in the original location of the light rays and an increase in illumination in the location at which the light ray is displaced. In this figure, this would result in location where the blue dotted line meets the viewing screen as a brighter illumination spot and its' original location of the orange line as a darker spot (provided that there is not another disturbance refracting to the position of the orange line on the viewing screen).

This method only observes the variations in lateral gradients of refractive index. While it is the deflection angle, ε, that conventional schlieren observes (Equations 2.4 and 2.5), it is the gradients of the deflection, $\partial\varepsilon/\partial x$ or $\partial\varepsilon/\partial y$, observed through shadowgraphy. This is also known as the second derivative, or the Laplacian, of the refractive index ($\partial^2 n/\partial x^2$ or $\partial^2 n/\partial y^2$) [13, 14].

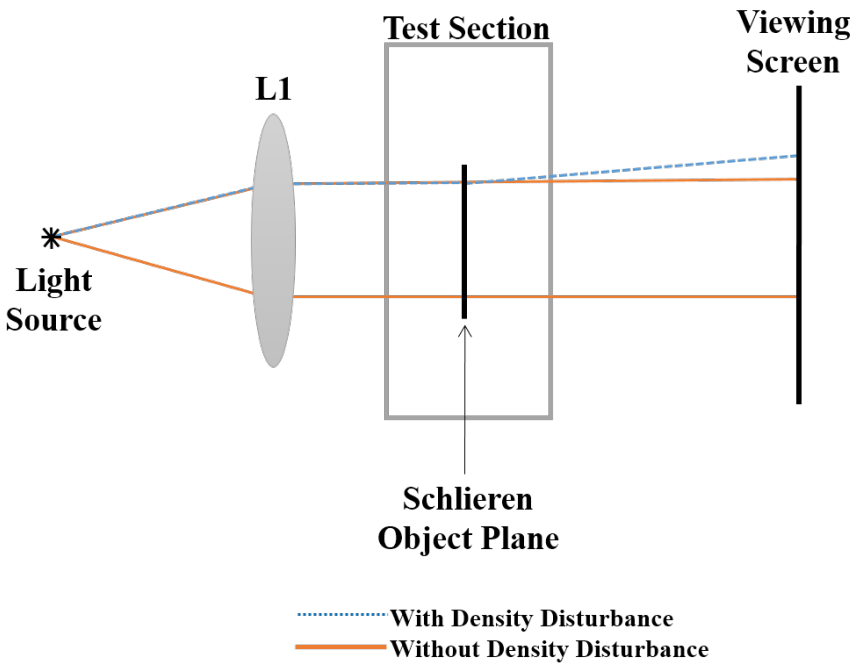

Figure 2.4: Schematic of a shadowgraphy setup using a point light source, a lens, and a viewing screen to project the light onto.

2.3 Background Oriented Schlieren

The BOS technique exploits the same concept that can be observed on a daily basis. Figure 2.5 shows the air surrounding a Blue Angel F/A-18 Hornet [1] that is distorting the shape of the building in the background. While it is known that the building is not actually this shape, this distortion has been created due to a density change in the air which relates to a refractive index change that an observer can visually see. This is also observable when driving down the road on a hot day and the stream coming off the pavement distorts the scenery in the far distance. Such examples use the same fundamental concepts that are used in an experimental setting with the BOS technique.

Figure 2.5: A Blue Angel F/A-18 Hornet [1] distorting the background during flight shows the same concept that the BOS technique exploits during an experiment.

The BOS technique was first proposed in a patent filed by Meier in 1999 [15] and is noted for its simplicity and ease of application. The technique requires only a few components: a camera, a patterned background, a light source, and a computer for image processing. BOS also has the advantage over other schlieren based techniques because it depends only on the size and detail of the background being used, which in theory allows for an unlimited field of view and size of monitored object [29, 14]. Figure 2.6 shows a schematic of a typical BOS experimental setup. A camera, represented here by a simple lens and image sensor, captures images of the background with (blue dotted line) and without (orange line) density disturbance between the camera and the background. The image without the presence of the disturbance is often referred to as the *reference image*. In the presence of the disturbance, density gradients in the flow will cause light rays propagating from the background to the camera to refract, thus appearing as a displacement of the undisturbed reference image. The location at which the density disturbance occurs is often referred to as *schlieren object plane*. This plane is assumed to be infinitely thin, where no other disturbances are observed between

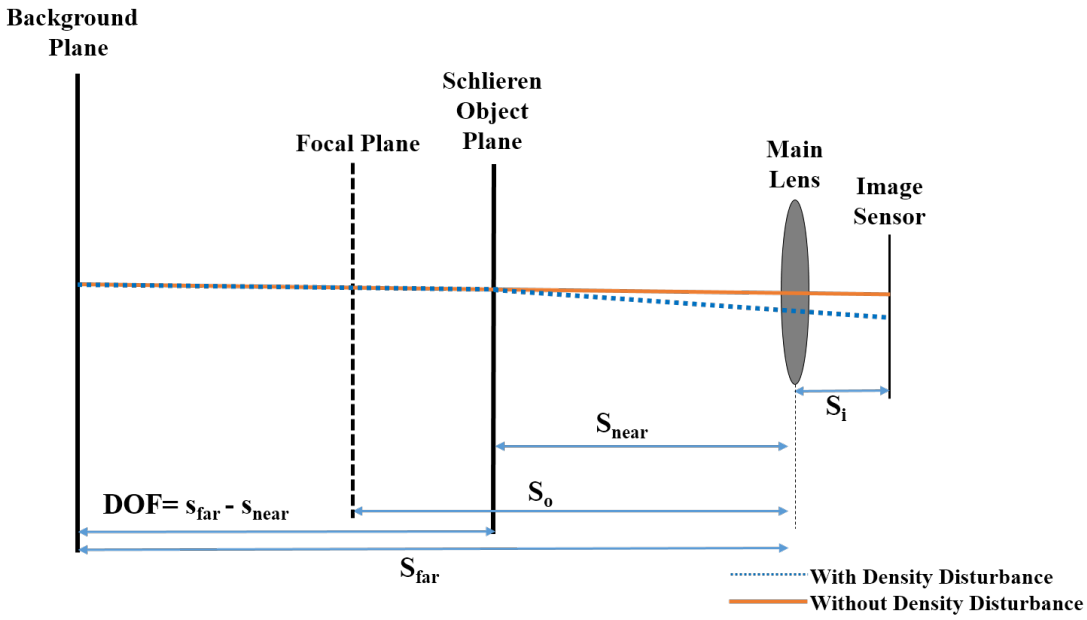

Figure 2.6: Experimental schematic of the BOS technique, where the camera is represented by a simple lens and image sensor. The disturbance is assumed to occur at an infinitesimally thin plane without any other disturbances occurring between the background and the camera. Adapted from Bichal [9].

the background and the camera. Figure 2.6 also provides the measured distances to each plane within the setup. The terms s_i and s_o are the image and object distances determined according to the thin lens equation. As will be discussed more in detail in Chapter V, the terms s_{near} and s_{far} define the region in front of and behind the focal plane that will appear to be in-focus. The entire region between these two distances, termed the depth of field (DOF), can be determined based on known camera parameters. While there are variations in the BOS setup, this schematic places both the schlieren object and the background planes are the near and far locations of the DOF. This is based on the work of Bichal *et al.* [30].

The measured displacement of the background is a function of geometry, which is observable in Figure 2.7. This schematic shows that the displacement observed on the image sensor can be traced back to the apparent shift in the background in object space, d_o, where the total angular deflection, ε, signifies the angular difference created due to the presence of a disturbance in the flow. The geometric relationship between ε and d_i can be represented

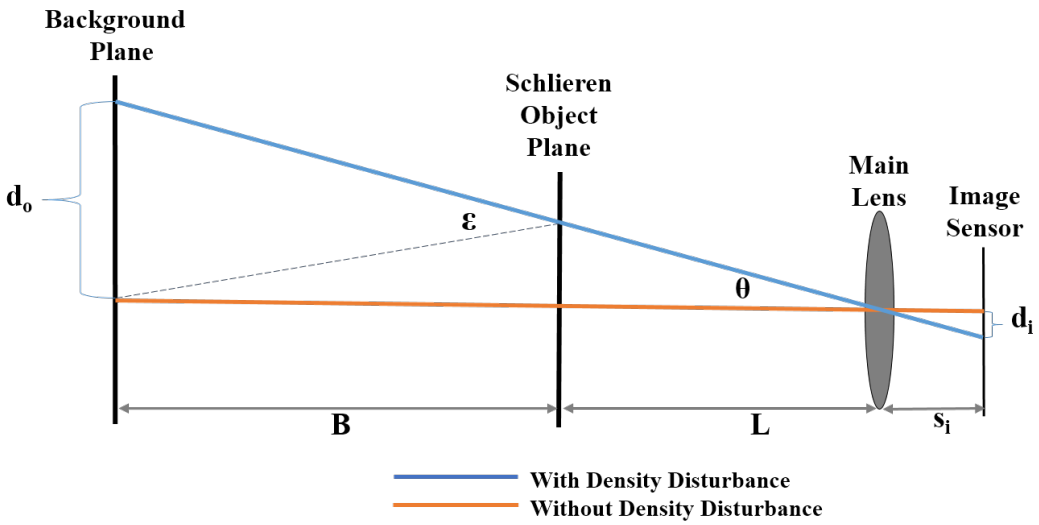

Figure 2.7: A schematic of the geometric relationships observed in a BOS configuration, where the displacement observed on the image sensor, d_i, can be traced back to an apparent shift in the background in physical space. The angle, ε, is used to calculate this shift in physical space based on known parameters for an experiment. Adapted from Bichal [9].

based on known parameters in a setup. This relationship is represented in Equation 2.6, where L is the distance from the main lens to the plane creating the density disturbance, B is the distance from the background to the density disturbance plane, and f is the focal length of the lens. L, B, and f are fixed values for a given experimental arrangement. Equation 2.6 makes the assumption that deflections are small enough to implement the paraxial approximation. To implement the paraxial approximation in this work's experiments, "small enough" means displacements no greater than a millimeter (mm) in physical space, which equates to deflection angles in terms of milliradians. For sufficiently small deflections, Equation 2.6 relates the refraction of light to the measured displacement, and is a function of depth based on the given experimental parameters. The sensitivity, or magnitude, of the measurable displacement decreases and the schlieren object plane moves closer to the background plane.

$$\varepsilon = \left(\frac{L}{B} + 1\right)\left(\frac{d_i}{f}\right) \tag{2.6}$$

The basic understanding of this geometric relationship and its' ability to provide a sensitive measurement are both well understood, though the optimal arrangement in an experiment to exploit this sensitivity is not as well understood to the scientific community. Some research groups have placed just the background in-focus and the schlieren object out of focus [16, 31, 32], while others have placed both the background and schlieren object in-focus [33, 29, 34]. Typically this variation in setups is a result of finding a compromise between the parameters required for the setup. This includes taking into consideration the length scale of the setup, the desired field-of-view, the available lenses to use for imaging, as well as the resolution of the camera and the background.

In a laboratory BOS setup, the background typically consists of a random pattern printed on a piece of paper; however, in the field, the background can be taken of natural objects with sufficient texture such as a forest, a section of a cornfield, or the concrete ground [35, 33]. Additional patterns in ground test facilities have been made with glitter spray paint, laser speckle projected on a retroreflective surface, and even crumpled aluminum foil [36]. Backgrounds are selected based on their high contrast and unique pattern features, both of which are important during the image comparison process in order to quantify the magnitude of the distortion.

This amount of distortion can be quantified by directly comparing the reference image to the distorted image using various image processing algorithms. The most common method to measure distortions uses 2D cross-correlation algorithms adopted from the Particle Image Velocimetry (PIV) community [37]. This algorithm is capable of determining the local magnitude and direction of the image distortion. The magnitude of the distortion is a line-of-sight integrated quantity that depends both on magnitude of the density gradient as well as its location relative to the camera and background. Without a priori knowledge about the depth at which refraction takes place, interpretation of the image distortion acquired with a single camera is generally limited to qualitative analysis with 3D aspects of the flow remaining most ambiguous.

The BOS technique has been used to explore several types of flow fields including the examples shown in Figure 2.8. These examples include the vortices being shed by helicopter blades [38], shock waves being produced by a test object in a supersonic wind tunnel facility [39], and thermal plume of a simple hand held lighter [40]. Though there are many more applications than just mentioned, it is important to note that this technique has been used on a wide ranges of length scales. A rather large length scale includes using the Sun's edge as a light source in a variation of BOS called Background Oriented Schlieren using Celestial Objects (BOSCO) in order to visualize the shock wave structures of a T-38C during flight [41].

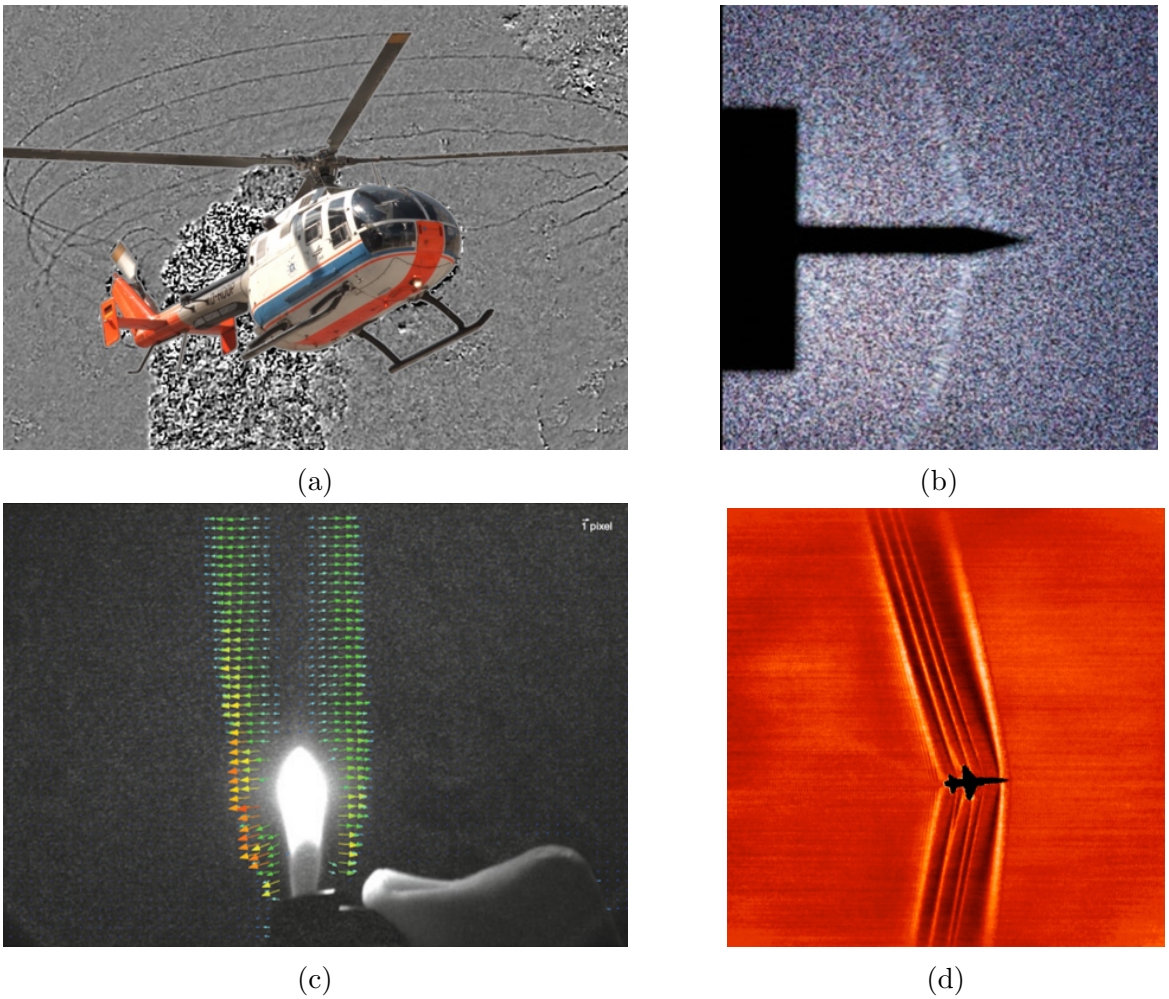

(a) (b) (c) (d)

Figure 2.8: Examples of the BOS technique used towards a wide variety of applications.

2.4 Focused Schlieren

A system known as a focusing schlieren system requires an extended light source, a lens, a camera, a source grid, and a cutoff grid. The source grid is typically made up of evenly spaced black and transparent lines placed closed together, and ideally the cutoff grid is the perfect negative of the source grid [17]. Similar to conventional schlieren, a grid consisting of horizontal lines will detect vertical deflections and vice versa. A schematic of this system using horizontal grid lines is shown in Figure 2.9, where this system is thought of as the superposition of many conventional schlieren setups. Each transparent strip in the source grid acts similar to that of the point source in a schlieren setup, and the corresponding black strip on the cutoff grid acts as the knife edge [2]. These systems also require that 50% of the incoming light rays get cut off by the cutoff grid.

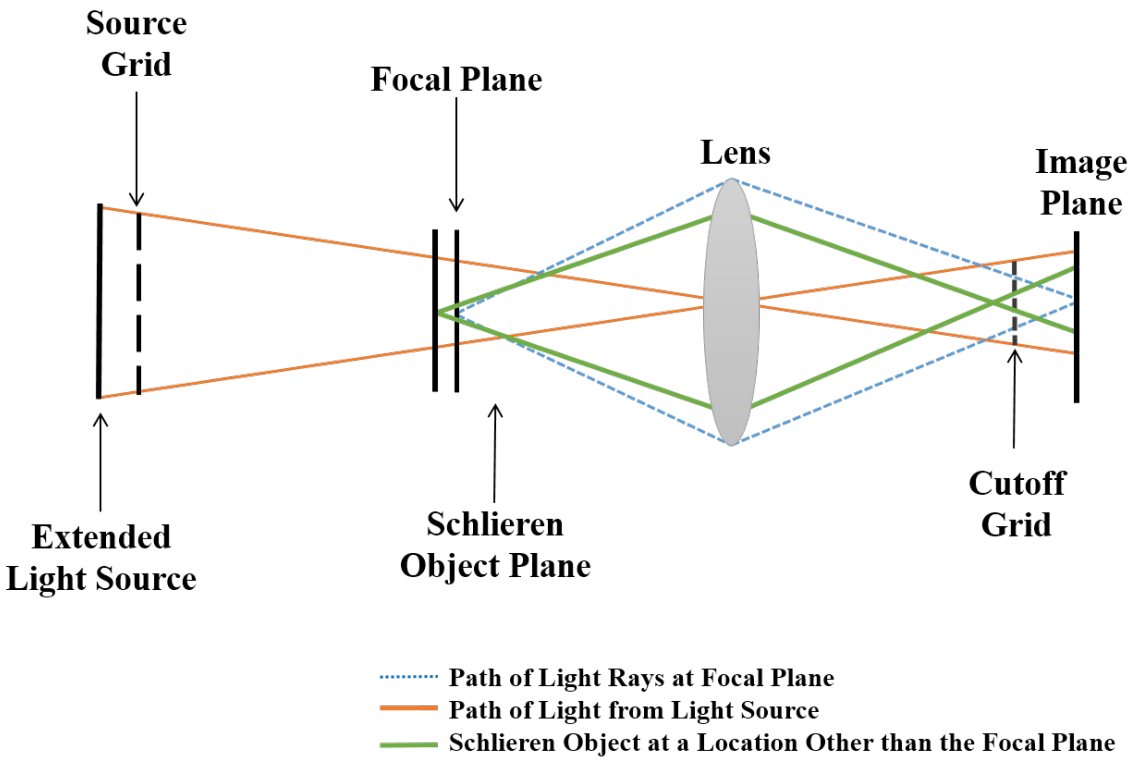

Figure 2.9: Schematic of a focused schlieren system with an extended light source channeling the light through a source grid and cutoff grid onto the image plane. Adapted from Goulding [17].

The uniqueness of this system lies in observing disturbances produced by the schlieren object relative to the focal plane position. As shown in Figure 2.9, refraction occurring at the focal plane of the imaging system will result in the a large brightness in a small region of the image sensor. Alternatively, refraction occurring at a location other than the nominal focal plane will result in small brightness spread across a larger region on the image sensor [17]. This idea follows the blue dotted and green lines respectively in Figure 2.9. An image resulting from a setup such as this will provide a focused 2D plane of a location within the test section, where the noise is reduced for out of focus disturbances.

As an example of images produced with this type of setup, Floryan *et al.* [2] used two jets produced by compressed air cans separated by 13 millimeters. Images of this type of setup are shown in Figure 2.10, where one jet is placed horizontally from the left and the other is place on a diagonal from the right. The two jets display in-focus features at different focal plane positions. Notice that the when the diagonal jet is out of focus, the variations in light are blurred across a region in the image. Significant details cannot be observed about the out of focus features. This is the same for position at which the horizontal jet is out of focus. It should be noted here that in order to obtain these two images, the focal plane had to be manually changed in order to acquire the desired in-focus position.

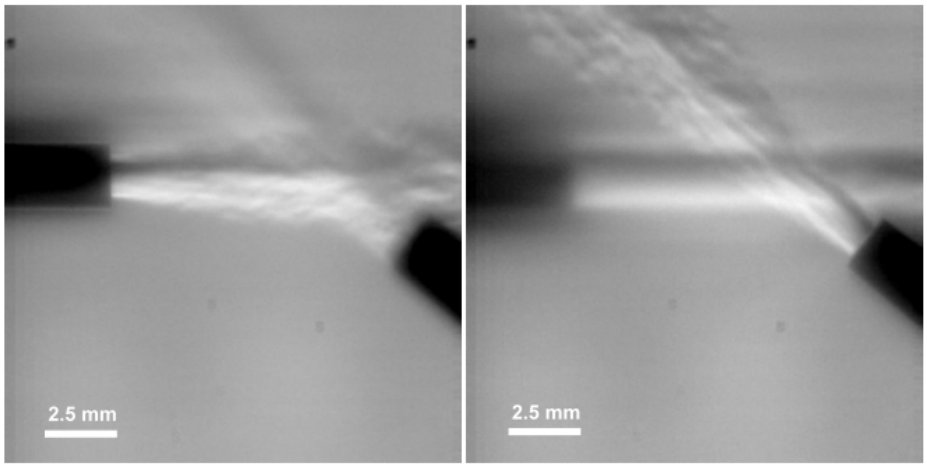

Figure 2.10: Results from an experiment performed by Floryan *et al.* [2] using two jets placed 13 millimeters apart.

2.5 Summary of Schlieren Techniques

Though the concept of schlieren has a long history, the class of schlieren imaging techniques has been expanded and improved upon alongside the many advancements made in technology. They are a common visualization technique that provide the ability to see the unseen. Schlieren provides a way to observe the refractive index gradients. Shadowgraphy provides a way to observe the second spatial derivative of the refractive index field. Background oriented schlieren is a technique that provides the ability to begin quantifying the inhomogeneities present in the refractive index field by using a simpler experimental arrangement. Focused schlieren, though complicated to setup, provides the ability visualize density disturbances located at the focal plane position without as much influence of other disturbances placed at alternative locations within the experimental volume. These are just some of the many variations of the original schlieren technique. With such a wide range of applications to be used towards, the use of these technique continue to be a staple in most flow visualization laboratories.

Chapter 3

3D Measurements Using Schlieren Techniques

While the family of schlieren techniques provide qualitative feedback with regards to flow field characteristics, there have also been many research groups who have explored different approaches to make both 3D and quantitative observations. The transition to these methods is motivated by the fact that most flows are inherently 3D, therefore 3D methods are needed in order to provide improved results of such situations. These common 3D methods shown in Figure 3.1 require either the rotation of the schlieren object to capture multiple projection angles (Figure 3.1a) or the use of a multi-camera configuration (Figure 3.1b). Two alternative methods will also be mentioned in this section, which provide unique approaches to obtaining 3D information.

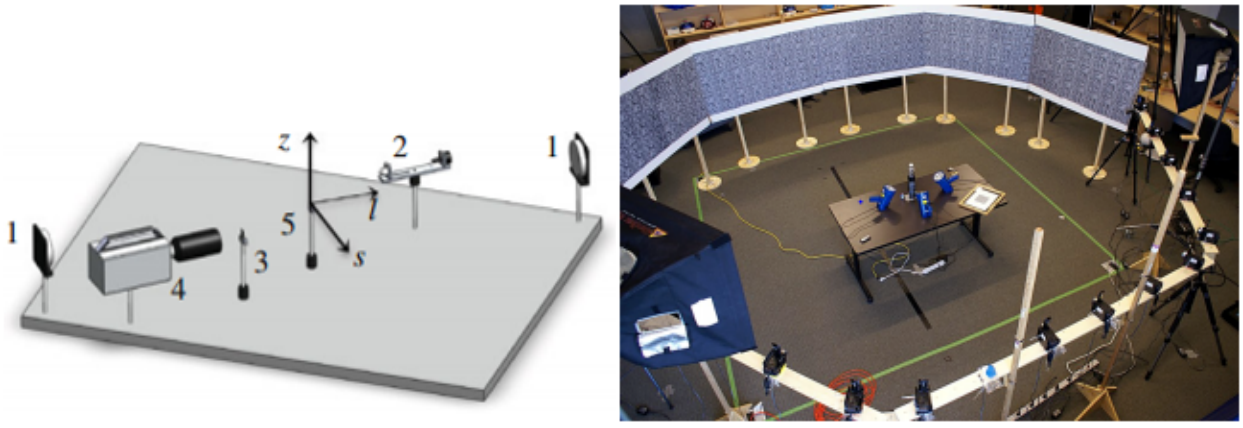

(a) (b)

Figure 3.1: Examples of the common setups used to obtain 3D information. (a) Rotating the schlieren object has been performed by Cabaleiro *et al.* [3] (b) A multi camera configuration has been used by Atcheson *et al.* [4].

The collection of multiple projection angles are used to perform a reconstruction. A common reconstruction algorithm used for this type of work is a computed tomography

method, which collects line-of-sight integrated measurements across the particular medium through a wide range of angles, or projections. With the focus of the current work being on the implementation of BOS, the following chapter highlights a few of the many approaches that have been taken to explore the three-dimensionality of several flow field problems using a BOS configuration. It is important to keep in mind that such approaches have benefits and trade-offs with respect to the experimental setup, the complexity of the reconstruction method, the amount of time required, and the cost of such experimental arrangement.

3.1 3D Measurements with a Single Camera BOS System

Single camera systems require either the rotation of the schlieren object or the change in position of the camera viewing the object in order to capture multiple projections of the desired flow field. Goldhahn and Seume [5] used 36 different measurement projections to observe an under-expanded free jet of air using a double hole orifice. Each projection angle required the manual adjustment of the jet, which required loosening four screws and adjusting the angle using an angular scale. At each of the 36 projections, 60 images were acquired in order to obtain average shift values for each projection. These average values were used in a tomographic reconstruction call the filtered back-projection algorithm (FBP) in order to generate a 3D density field. The algorithm uses planes perpendicular to the jet axis and takes each horizontal pixel line coming from the projections to retrieve a slice of the jet. Though the details of such reconstruction are beyond the scope of this work, the density distribution determined from the reconstructed planes provides the ability to build a measurement volume. The density distribution is shown for three different slices determined through this method, where (a) is a slice along the jet axis, and both (b) and (c) are two different slices in the z-plane.

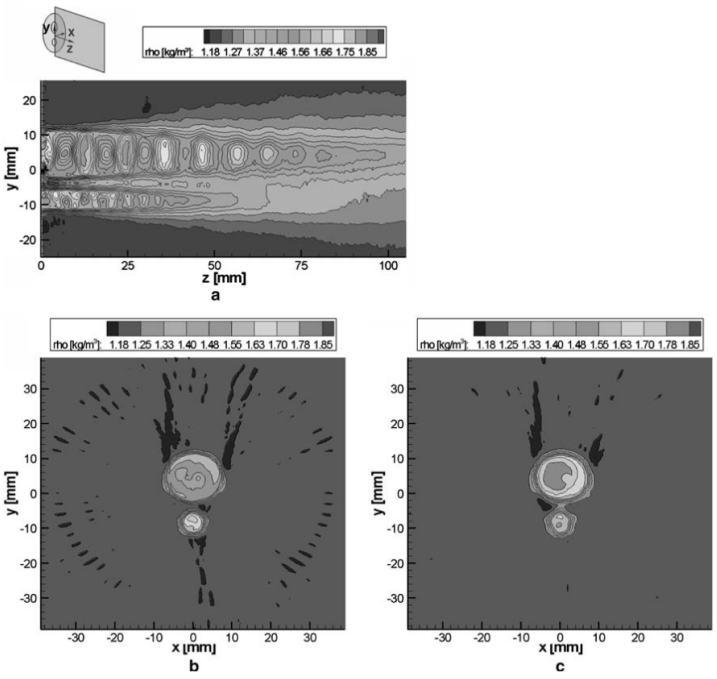

Figure 3.2: The density distribution of an under-expanded free jet of air using a double hole orifice reported by the work of Goldhahn *et al.* [5], where (a) is a slice along the jet axis and both (b) and (c) are different slices in the z-plane.

A different approach to a single camera configuration was explored by Ota *et al.* [6, 20], This approach used the Colored-Grid BOS (CGBOS) technique, which consisted of a background made up of green horizontal stripes and red vertical stripes. At 19 different projections, images were acquired of an asymmetric model placed in a supersonic wind tunnel. Displacements of the stripes caused by the formation of a shock wave were measured obtaining a finite-fringe interferogram though the use of the Laser Interferometric Computed Tomography (LICT) measurement. Once the displacement data was obtained for each of the projection angles, the Algebraic Reconstruction Technique (ART) was used for reconstruction. ART is an iterative reconstruction method, and can use less projections to perform a reconstruction compared to that of the FBP algorithm. This experiment contains incomplete projection data due to the light being cut off by the asymmetric body itself. The refractive index gradient distribution was determined with this reconstruction method without a complete set of projection data. In order to obtain the refractive index distribution, a Poisson

solver is used alongside the Successive Over Relaxation method. Using the refractive index distribution alongside the Gladstone-Dale relation, the normalized density distribution was determined. An example of the 3D results determined from this experiment are shown in Figure 3.3. The image on the left shows the density distribution along the central plane of the system, and the image on the right shows the 3D density distribution and the surfaces possessing constant density. Both of these images highlight the features created by the asymmetric body in a supersonic flow in both a qualitative and quantitative manner.

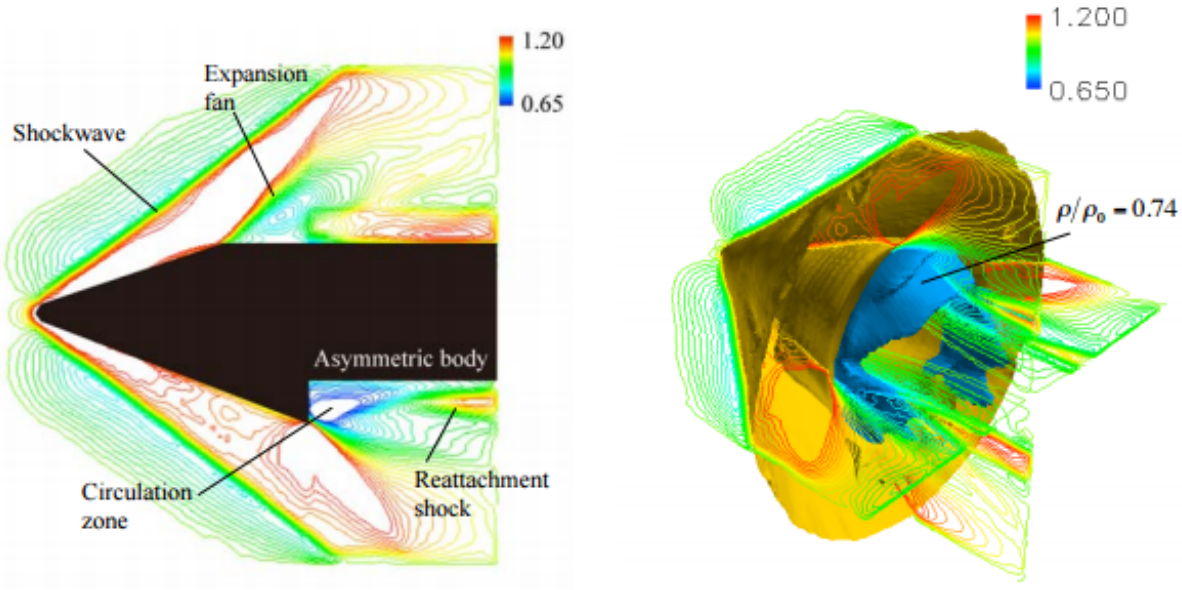

Figure 3.3: Results of an asymmetric model placed in a supersonic wind tunnel reported by the work of Ota *et al.* [6]. A single slice of the density distribution is shown along central plane of the asymmetric body on the left, and the 3D density distribution is shown alongside surfaces possessing constant density on the right.

While these two experiments have been confined to a simple summary, the amount of detail compacted into these explanations shows the amount of detail required to successfully implement a 3D reconstruction with a single camera. Though this approach would be favorable with facilities possessing limited optical access, this type of setup is disadvantageous in experiments where time-resolved data is desired. This is not quite possible with this type of setup due to the capture of a single projection at a single instant in time.

3.2 3D Measurements with a Multi-Camera BOS System

Multi-camera configurations in a BOS setup require the additional complexity of a calibration step to ensure that each imaging system is capturing the same region of interest in a BOS setup. Camera alignment and calibration are important steps in being able to merge together all the measured distortions from different viewing angles. Through there are several approaches to this calibration problem including the work of Le Sant *et al.* [42]. Their work provided a method that is capable of calibrating up to 12 different cameras for a particular BOS setup.

With respect to obtaining BOS measurements from multiple cameras to obtain 3D density reconstructions, Atcheson *et al.* [4] used a 16 camera configuration to capture information about several examples of non-stationary gas flows. Their method first calibrated all 16 high-definition consumer cameras placed in a 180° arc surrounding the desired field of view. Deflection measurements were determined for each camera's view for each instant in time through the use of optical flow algorithms. Such information was then used in a novel tomographic technique developed by this research group, which uses a visual hull constraint in the reconstruction process. The visual hull used to perform a 3D reconstruction required the creation of a binary mask for each camera during each instant in time. Such visual hull was then used to guide the tomographic reconstruction, which provided the ability to generate a 3D reconstruction of the refractive index gradient field as well as the density gradient field using a Poisson solver. Examples of a reconstruction performed on several instances in time are shown in Figure 3.4 of a turbulent flow of hot air produced above a gas burner. The 3D features were qualitatively observed over a known time frame, and this experiment provided the first volumetric time-resolved BOS system.

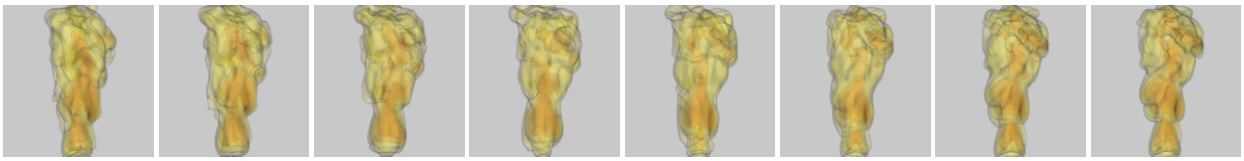

Figure 3.4: Volumetric time-resolved results reported by the work of Atcheson *et al.* [4] of a hot air plume above a gas burner.

A more recent 3D BOS setup used 12 cameras in an experimental setup surrounding a underexpanded jet. This work was performed by Nicolas *et al.* [19, 7]. Their work used the multi-camera calibration from the work of Le Sant *et al.* [42], acquired the BOS measurements from the use of 12 cameras, measured the displacement values associated with each camera position, and then converted the 2D displacements into a 3D angular deviation. Such deviations were determined to be valid or not with the use of a 3D mask developed from the collection of 2D masks created by each camera's view. This validation was used to determine whether the deviations were considered within the volume of interest or not in order to generate the appropriate numerical reconstruction of the density field. This research group tested this method on four different convective flows to assess the reconstruction of both simple and complex 3D structures. One of the convective flows was the plume of a candle. The 3D density field reconstruction of this flow alongside a planar slice in the (y, z) plane and the (x, y) plane are shown in Figure 3.5. Such results were consistent with the knowledge of the evolution of a plume, and this approach presented a new reconstruction method to determine the 3D density field from BOS measurements.

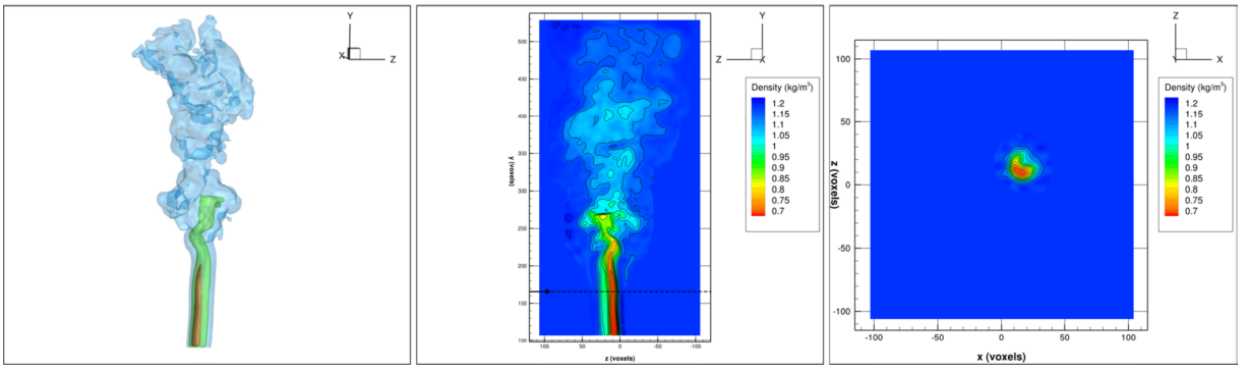

Figure 3.5: Results reported by the work of Nicolas *et al.* [7] The left image shows a 3D density reconstruction, the center image shows a (y, z) plane slice, and the right image shows a (x, y) plane slice of the plume of a candle.

As stated the previous section, the detail of these experiments shows the complexities encompassed in the setup of a multi-camera configuration. Though complex in nature, these multi-camera configurations have provided a successful way to collect 3D information about the desired flow field. This success comes with several trade-offs including the an increase in setup time, an increase in laboratory space for such a configuration, and an increase in expenses due to the need for multiple cameras. Such factors are important to take into consideration for a particular experiment.

3.3 3D Measurements with a Light Field Probe

An alternative approach to capturing 3D information in a single image has been preliminarily explored by Wetzstein *et al.* [8]. Their work used a single camera imaging the distortions with the placement of light field probes behind the object creating the distortion. The use of two different light field probes were explored, where the first was a lenticular sheet with cylindrical lenses and the second was a hexagonal grid of spherical lenses. These probes were mounted to a light box placed behind the object creating distortion alongside a filter that was used to observe the refraction of light in a particular manner. This work explored several different types of filters including a spatio-angular filter. This type if filter encodes the two-dimensional angular dimensions and one spatial dimension in terms of three

color primary gradients. An example of the results is shown in Figure 3.6, where the object providing refraction is a pineapple shaped transparent plate. This use of the spatio-angular filter provided the ability to obtain the vertical ray displacement (top, right image of Figure 3.6) as well as a horizontal and vertical per-pixel refractive index gradient (bottom images of Figure 3.6). These results though preliminary seek to explore the use of such spatial and angular information to reconstruct a 3D refractive index field.

While this approach has been successful in capturing both spatial and angular information about the scene in a simple setup, this technique has been limited to solids and liquids. Slight refractions occurring in gas flows require an increase in precision and sensitivity of the system; both of which this setup currently lacks. This is due to the use of off-the-shelf hardware rather than specialized equipment that could potentially provide the appropriate setup for observation of much smaller deflections occurring in gas flows.

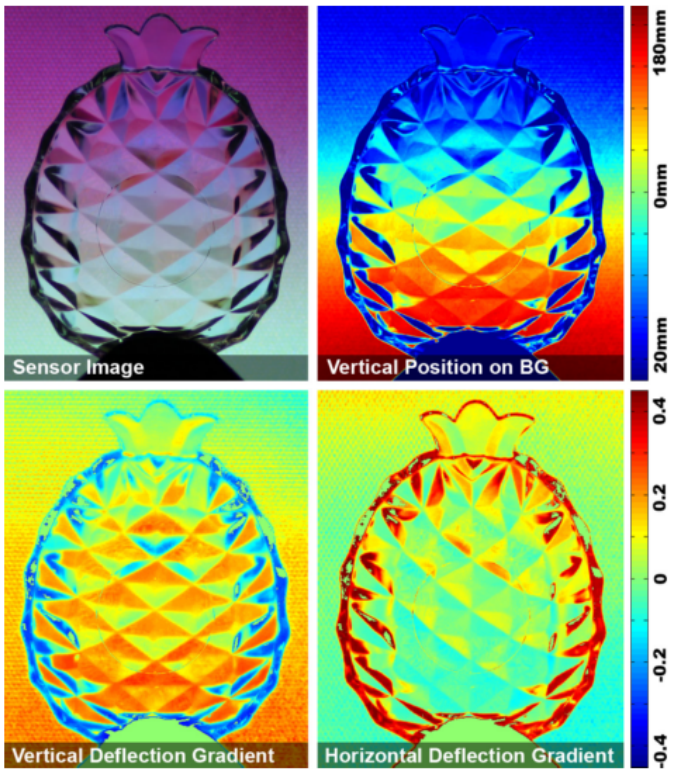

Figure 3.6: Results reported by the work of Wetzstein *et al.* [8], where a spatio-angular filter helped to determine the vertical ray displacement and the horizontal and vertical refractive index gradients per-pixel.

3.4 3D Measurements with a Single Plenoptic Camera BOS System

The work most closely related to the work presented in this thesis has been performed by Abhishek Bichal [9]. He preliminarily explored the integration of a plenoptic camera into a BOS experimental arrangement. His work used the capabilities of the plenoptic camera to gain 3D information about a conical shock wave in the supersonic wind tunnel facility at Auburn University. While the capabilities of the plenoptic camera are discussed in a later section, it is important to note that this was the first time any researcher has tried to perform this type of experimental configuration. Rather than taking the common approach of exploiting the refraction of individual light rays, he determined the sensitivity of his BOS setup based on exploiting the light as a wavefront.

In his work, Bichal defined a 3D Density Measurement Technique (3DDMT), used to reconstruct the volume of the flow field within the supersonic wind tunnel facility. His work used both experimental and simulated data in order to explore the reconstruction method, which used the multiple projections obtained from the plenoptic camera towards a tomographic-based algorithm known as the Multiplicative Algebraic Reconstruction Technique (MART). Both simulated and experimental data matched well visually when looking at single slices of the density distribution within the volume. An example of this is shown in Figure 3.7, where the simulated result is on the left and the result from the experimental data is shown on the right. These results represent the slice in the volume relating to the focal plane location of the experiment, where the shock is observed to be sharpest within the volume.

From this work, several key concepts were discovered/explored. First, the ability to use multiple projections to determined the position of the shock and the cone within 3D space were successfully determined with less than 3% error. Second, the use of the projections obtained from a single plenoptic camera did not provide enough angular disparity to accurately reconstruct the volume. Though there were successful comparisons made between the results generated from the simulated and experimental data, there is motivation to explore the

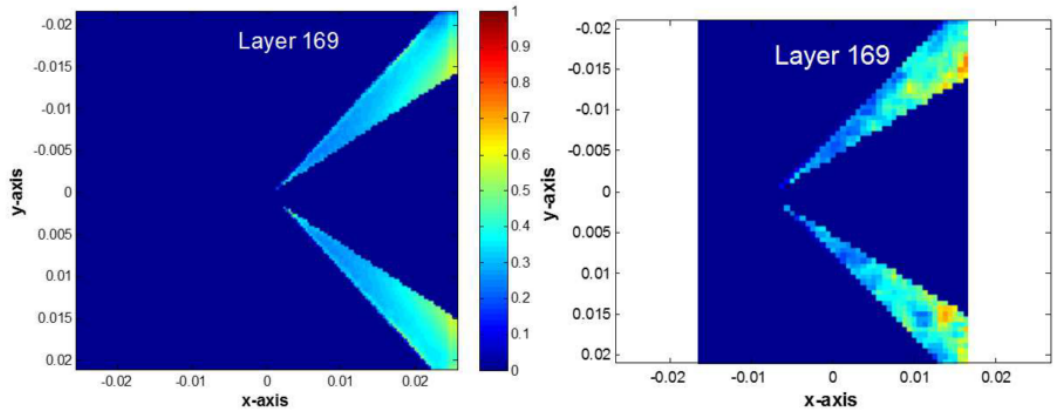

Figure 3.7: Results reported by the work of Bichal [9] showing a visual comparison of the density distribution determined from simulated data (left) and experimental data (right) for a single slice within the volume.

combination of the plenoptic camera with the BOS technique with regards to the 3DDMT in order to develop a more accurate reconstruction of the volume. Further development of this method includes the used of more projection angles, the presence of more than one disturbance in the flow, and the use of alternative image processing algorithms such as optical flow algorithms.

3.5 Summary of 3D BOS Methods

There have been several 3D BOS approaches discussed in this section. Each approach has its' own complexities when incorporated into a particular setup in order to obtain successful results. A single conventional camera BOS arrangement hinders the ability to acquire time-resolved data, and it also has the inherent complexity of manually changing the schlieren objects position relative to the camera. A multi-camera configuration requires a cumbersome alignment and calibration process in order to ensure that all cameras are viewing the same desired region of interest. This is not often favorable in labs with limited space or limited optical access. The BOS arrangement with the light field probe is currently limited to solid and liquid disturbances, which hinders the use of this approach in gaseous flows. The use of a single plenoptic camera in a BOS arrangement has been preliminarily explored, yet there are

several complexities to this arrangement that require a much deeper level of investigation. The current work in this thesis is be aware of the work performed by Bichal [9], and use such knowledge to fill in the gaps that are not well-understood up to this point. This includes using the unique capabilities of the plenoptic camera, gaining a greater understanding of the results that a BOS setup with a plenoptic camera produces, as well as knowing the limitations of this arrangement in order to progress towards the ultimate goal of reconstructing a 3D density field in the future.

Chapter 4

Light Field Imaging and a Plenoptic Camera

4.1 History of the Plenoptic Function and the 4D Light Field

The term *light field* was first formally defined by Gershun [43] in 1936, though the idea of describing the way rays of light fill the world with information dates back to Leonardo da Vinci's observations. da Vinci viewed the world as a collection of an infinite number of light ray bundles that filled all the regions of space, where each bundle was defined as a "radiant pyramid." Several centuries later, such a concept inspired the development of the plenoptic function by Adelson and Bergen [21], which is a function used to uniquely define a light ray in terms of seven different parameters. Every possible viewing angle (ϕ, θ) for any wavelength of light (λ) at any given time (t) at any viewing position in Cartesian coordinates of a region in space (V_x, V_y, V_z,) provide the parameterization of plenoptic function shown in Equation 4.1. Such an equation, according to Adelson and Bergen, defines objects and how they fill space through patterns of light rays.

$$P = P(\phi, \theta, \lambda, t, V_x, V_y, V_z) \tag{4.1}$$

With the notion that seven dimensions are required to characterize the light field, the plenoptic function is an idealized equation in this form. This equation conceptually represents how the light field can be structured to provide information about a scene but does not provide an approach to physically measure all wavelengths of light from every viewing angle at every instant in time. Equation 4.1 can be reduced to five parameters if all wavelengths

are averaged for a given instant in time, which is represented by Equation 4.2. The parameterization of the light field in five dimensions (5D) can represent a scene according to Figure 4.1a in terms of three spatial coordinates (x, y, z) and two angular coordinates (ϕ, θ) [10]. As long as nothing occludes the path of the light ray, the function can be further reduced to four parameters because the intensity of the light will remain constant along the light ray. Levoy and Hanrahan [44] proposed this four-dimensional (4D) parametrization in terms of a light ray intersecting with two planes: (u, v) and (s, t), which are represented in Equation 4.3 and also shown in Figure 4.1b. The light ray itself can be defined by the location at which is passes through both planes. The value of the function, L, is the irradiance of the light ray given by the coordinate four coordinates: u, v, s, and t. This 4D parameterization is used for the current work's discussion.

$$L = L(\phi, \theta, V_x, V_y, V_z) \tag{4.2}$$

$$L = L(u, v, s, t) \tag{4.3}$$

4.2 The Plenoptic Camera and Its' Capabilities

Though there have been several approaches to capturing the light field, the basis of this research emanates from an idea that was first suggested by Lippman in 1908 [45]. He proposed a camera configuration with the addition of small lens array (microlens arrays) in front of the image sensor. Due to the lack of technological capabilities at the time, this remained only an idea until Adelson and Wang [22] constructed a plenoptic camera using a lenticular array made up of approximately 100×100 microlenses and a relay lens to project light rays onto the 512×480 pixel image sensor of a digital camera. With further advancement of the digital imaging capabilities, Ng *et al.* [11] constructed the first hand-held plenoptic

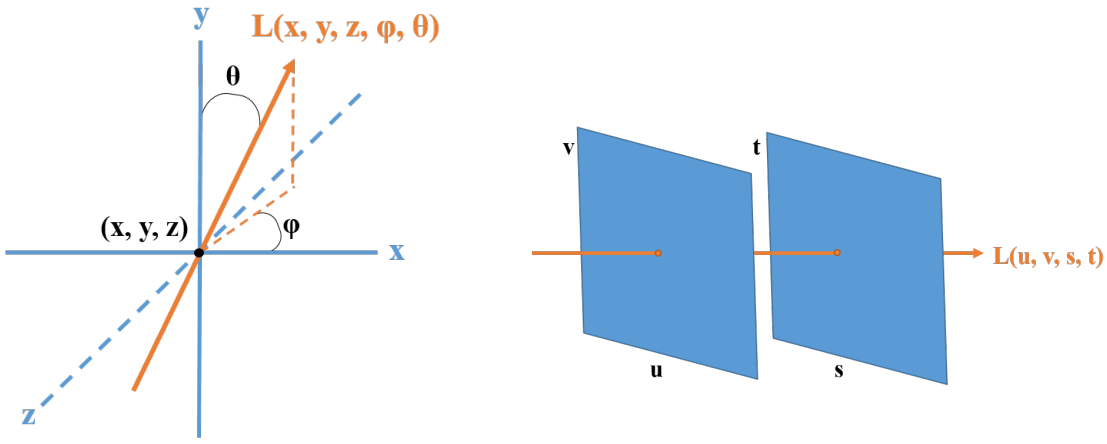

(a) *5D Parameterization* (b) *4D Parameterization*

Figure 4.1: (a) Schematic of the 5D parameterization of the light field in terms of three spatial coordinates and two angular coordinates. (b) The redundancy of one spatial coordinate is eliminated based on the assumption that nothing is occluding the light ray's path. This schematic shows the 4D parameterization of the light field as it intersects with two planes: (u, v) and (s, t). Both schematics adapted from Levoy [10].

camera using a rectangular microlens array made up of 296×296 microlenses and a 16MP camera.

A camera configuration with the addition of a microlens array is shown in Figure 4.2. Light emanating from a point source at the focal plane passes through the main lens, maps to a specific location on the microlens plane, and projects onto different pixels on the image sensor. Figure 4.2 simplifies the total light ray distribution from that location by showing five subsets of light rays represented by the five different colors. These subsets represent the different angles at which the light rays are traveling and can be represented by both the pixel location and the microlens plane location using the concept of the two-plane parameterization. This parameterization provides the ability to uniquely record the intensity of each light ray on the image sensor. The pixel represents the angular information about the light field in terms of (u, v) coordinates, and the microlens plane location represents the spatial information in terms of (s, t) coordinates. With the ability to classify each light ray in terms of spatial and angular coordinates, there are two unique capabilities that can be

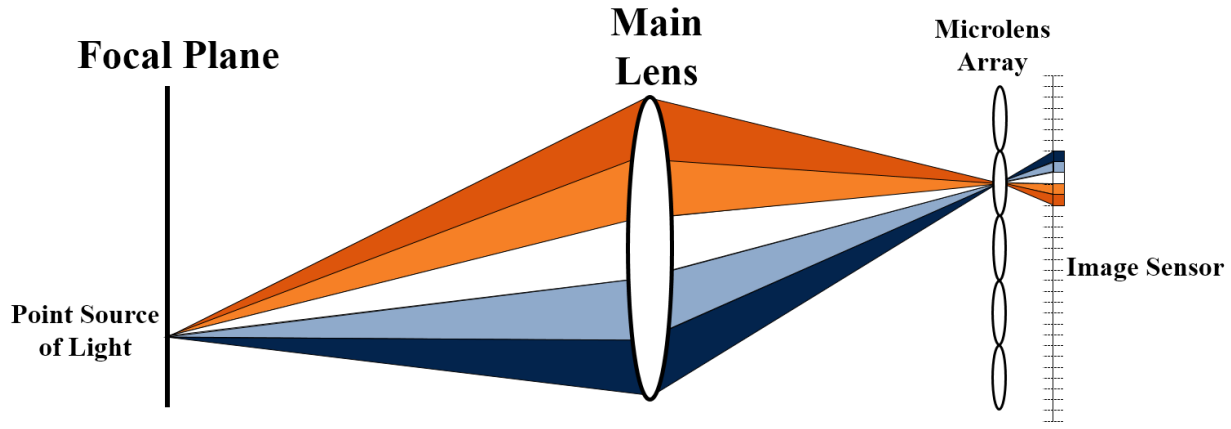

Figure 4.2: Schematic of the components that make up a plenoptic camera. Light rays emanating from a point source at the focal plane with pass through the main lens, through a specific microlens, and depending on their angle, project onto different pixels on the image sensor.

computationally performed after a plenoptic image is acquired: the ability to change the perspective view and the ability to change the focal plane.

The ability to render a synthetic image from different perspectives is performed by selecting a (u, v) coordinate that represents a specific location on the main lens plane and using all of the light rays that passed through the specified location. Figure 4.3a shows a schematic of this concept in a one-dimensional manner, where a single u coordinate corresponds to specific pixel locations behind all of the s coordinates or microlenses. In selecting a different u value (or u, v values in 2D), the perspective will shift accordingly based on the designated pixel locations. The schematic in Figure 4.3a also shows that rendering a single perspective view is effectively selecting a small portion of the main lens aperture. Using such a small portion of the aperture results in large depth of field, which will be discussed more in detail in a later section.

As a simplified example of this concept, a plenoptic camera with a microlens array of 2×2 microlenses is shown in Figure 4.3b. In order to generate a single perspective view, the same (u, v) value is chosen behind each microlens to form the desired image. The spatial resolution of a rendered perspective view is determined by the size of the microlenses, or spacing in samples of the chosen (u, v) coordinate. This can be mathematically represented

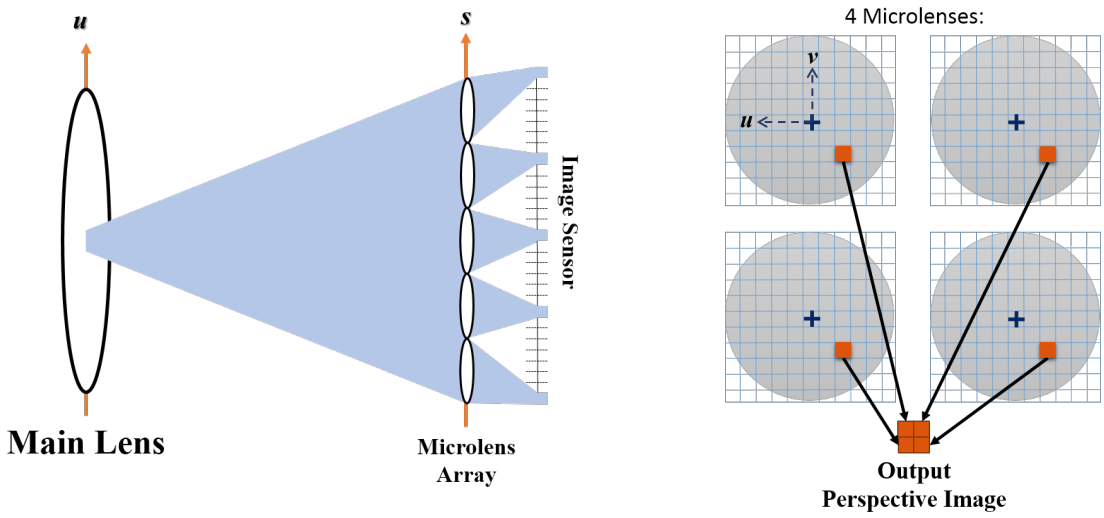

(a) (b)

Figure 4.3: (a) A schematic showing how a specific portion of the main lens corresponds to a single pixel behind each microlens that that used to render a perspective image. Adapted from Ng *et al.* [11]. (b) A plenoptic camera consisting of only 4 microlenses in the array generates a single output perspective image by choosing the same pixel location from behind each of the 4 microlenses.

by Equation 4.4, where the synthetic output image $I_{perspective}$(s', t') is rendered for a specified u_o and v_o for all s', t' values. The primed values signify the synthetic film plane location used to generate the desired perspective view.

$$I_{perspective}(s', t') = L\left(u_o, v_o, s', t'\right) \tag{4.4}$$

The camera used in this work's experiments is a custom camera designed and constructed by the Advanced Flow Diagnostics Laboratory (AFDL) at Auburn University. An Imperx Bobcat B6620 29MP camera with a KAI-29050 CCD image sensor has been modified with a 471×362 hexagonal microlens array. Each microlens has a pitch of 77 micrometers (μm) and a focal length of approximately 308 μm. The image sensor is 6600×4400 pixels with a pixel pitch of 5.5 μm. A raw plenoptic image has a resolution based on the microlens array, which is .077 mm/pixel. An example of a raw image is shown in Figure 4.4. Aliasing is present in this figure due to the down-sampling of a 29MP into an image format suitable for

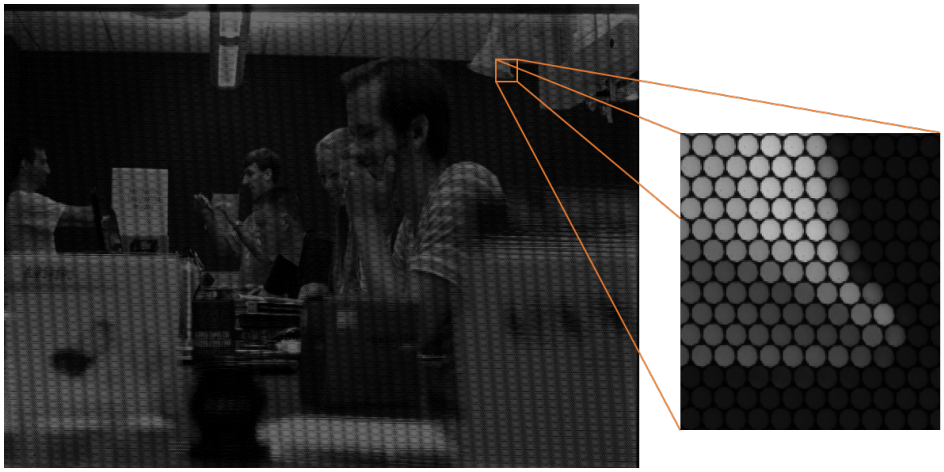

Figure 4.4: An example of a raw plenoptic image, where aliasing is present due to the downsampling of a 29MP image to fit the format of this document. A zoomed in portion of the image is shown on the right, where individual microlenses are observed.

this document. The right of Figure 4.4 is a zoomed in portion of the raw plenoptic image, which shows the sub-aperture images formed by a region of microlenses in the hexagonal array. These sub-aperture images are circular even though the microlenses themselves are hexagonal due to the light rays initially being captured by a circular aperture on the main lens.

While the raw plenoptic image has a spatial resolution of 6600×4400, the spatial resolution of a rendered perspective image is thus the number of microlenses in the array. This trade-off in spatial resolution is a result of gaining the ability to generate over one hundred perspective views from a single raw plenoptic image. Two sample images rendered from the raw plenoptic image are shown in Figure 4.5. These sample images were rendered using the Light Field Imaging Toolkit (LFIT) [46], which is an open source compilation of MATLAB functions created by the AFDL that is used to process plenoptic images. In these examples, the shift in perspective is most apparent when observing the letter E on the IMPERX box in the far right of the image and the R on the Auburn sign above the box. The edge of the text is obstructed in one of these views and not the other. It should be noted at this time that in order to generate perspective images appropriately, a calibration function in the

(a) (b)

Figure 4.5: Examples of rendered perspective view images. A leftmost perspective view is shown on the left and a rightmost perspective view is shown on the right.

LFIT determines the microlens centers in order to be able to appropriately select a u_o and v_o for a desired view.

Alongside the ability to shift perspectives, a raw plenoptic image can also render a synthetic image that has shifted the focal plane to a specified depth location within the scene. Figure 4.6 is a schematic representing this capability in a one-dimensional view. The light field can be resampled such that the image sensor is virtually placed at a different location, s'. Using the thin lens equation, the terms s_i, s_o, s'_i and s'_o represent the image space and object space distances according to light field collected at the original film plane and the new synthetic film plane, respectively. This synthetic film plane location is defined as $\alpha\ s_i$, where α represents a scalar value used to calculate the relative depth of the synthetic film plane with respect to the original film plane location. The light field actually recorded can be interpolated such that all the light rays passing through a synthetic point on the new film plane can be determined. To render a refocused image at this new film plane, the total angular information contained within the original light field is integrated such that each microlens is a sum of all the angles it possesses. This summation is mathematically represented in Equation 4.5, where $\mathrm{I}_{refocus}$ represents the synthetically refocused image for a specified α value. When α is greater than 1, the synthetic film plane is farther than the

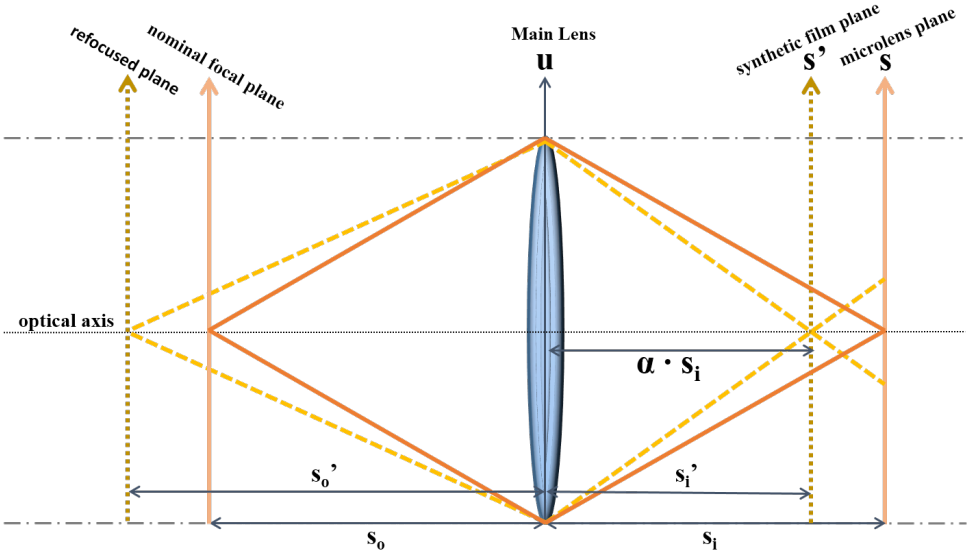

Figure 4.6: Schematic of the ability to synthetically change the focal plane from the original nominal focal plane in the raw plenoptic image. The new synthetic film plane is represented by $\alpha\ s_i$, where α defines the relative depth of the new plane with respect to the original plane.

original film plane, and vice versa when α is less than 1. Ng *et al.* [11] provides a more elaborate derivation of both Equations 4.4 and 4.5.

$$I_{refocus}(s',t') = \iint L\left(u, v, u + \frac{s'-u}{\alpha}, v + \frac{t'-v}{\alpha}\right) du\, dv \tag{4.5}$$

Using the same raw plenoptic image from Figure 4.4, examples of rendered images at different focal planes can be observed in Figure 4.7. The image on the left, Figure 4.7a is focused in the near field, where a lot of the far field information is blurred out and only details of the Auburn sign and *IMPERX* box in the near region are observable. The image on the right, 4.7b is focused in the far field, where details about the students are clear and observable. The generation of these images effectively uses the full aperture, which provides a very narrow depth of field, which will be further discussing in the following section.

(a) (b)

Figure 4.7: Examples of two refocused images rendered by using $\alpha = 1.15$ on the left to synthetically place the focal plane closer in the scene and by using the nominal focal plane with $\alpha = 1$ on the right.

Chapter 5

Depth of Field

In an imaging system, there is a finite distance in front of and behind the nominal focal plane that appear to be in-focus, known as the depth of field (DOF). As distance is increased from this in-focus range, objects gradually become more blurred. Mathematically, the DOF can be determined for a given scene by determining the near and far depth limits. As outlined by Kingslake [47]. Eqs. 5.1 and 5.2 show that these limits can be determined based off parameters that are fixed for a particular scene/setup.

In these equations, d_a is the diameter of the main lens aperture, s_o is the object plane distance, and c_o is the circle of confusion in object space. The DOF is the difference between s_{near} and s_{far} as shown in Equation 5.3. Using these equations for three different focal length lenses, the relationship between s_o and the DOF is shown in Figure 5.1. This figure uses the same circle of confusion for all three lens types (5 pixels with a pixel diameter of 5.5 μm). As the value of s_o increases, the DOF increases as well. It is important to note relationships like this when setting up an experiment in order to know where objects will appear clear and in-focus.

$$s_{near} = \frac{d_a s_o}{d_a + c_o} \tag{5.1}$$

$$s_{far} = \frac{d_a s_o}{d_a - c_o} \tag{5.2}$$

$$DOF = s_{far} - s_{near} \tag{5.3}$$

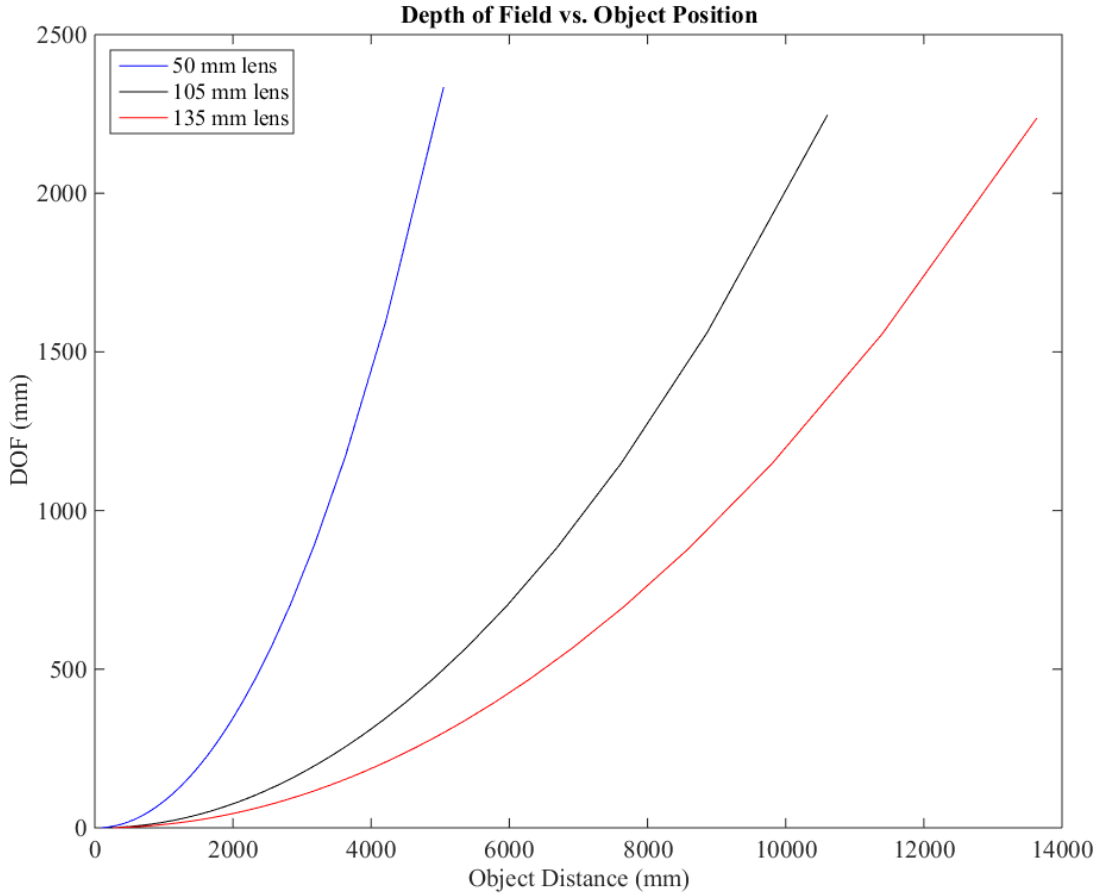

Figure 5.1: Relationship between object distance and the DOF for three different lenses.

For a BOS setup in a laboratory setting, there are several viewpoints as to what the optimal arrangement is for the positioning of the schlieren object, the focal plane, and the background. The sensitivity of the system, or how small of a density gradient can be detected, heavily depends on the optical arrangement of an experiment. This concept was discussed more thoroughly in Section 2.3. Bichal *et al.* [30] determined that the sensitivity of a system is directly proportional to the f# and circle of confusion for a set magnification. Both of these parameters play a factor in the determination of the overall DOF. As these values increase, the DOF also increases. Using this knowledge with regards to the depth of field equations, an experimental arrangement places the background at the back most plane in the DOF and the Schlieren object at the closest plane in the DOF [9]. This type of arrangement

is represented in Figure 2.6, where the distances to measurable values can be calculated to determine the appropriate DOF for a given set of experimental and camera parameters.

Before incorporating a plenoptic camera into a BOS experiment, it is important to understand the DOF associated with this imaging system. A rendered perspective view or refocused image from the raw plenoptic image data has an effective spatial resolution equivalent to the number of microlenses in the array rather than the dimensions of the pixels on the image sensor. Figures 4.5 and 4.7 show the influence of the DOF in generating perspective and refocused images, respectively. A perspective view is generated by selecting the same pixel location from behind each microlens, which is effectively selecting a small portion of the main lens. With a small aperture size, similar in theory to a pinhole camera, the DOF in this image type is large. Figure 4.5 shows this concept through the entire scene appearing to be in-focus regardless of the perspective view. A refocused image integrates over all of the information contained behind each microlens, which effectively uses the full aperture. Using a full aperture creates a narrow depth of field, as shown in Figure 4.7, where objects far from the focal plane are blurred and unclear.

Chapter 6

Background Oriented Schlieren with a Plenoptic Camera: Plenoptic BOS

6.1 Basic Concept

In conventional imaging, it is the intensity that forms an image where all light sources along the line-of-sight are integrated and recorded by the pixel values. In BOS, it is the displacement, which is a vector, that represents the data where all deflections are integrated along a line-of-sight. This vector is produced by measuring the image distortion as a function of position on the image sensor. In a plenoptic camera, multiple views are collected and multiplexed onto a single image sensor. A light field equivalent representation of BOS data with a plenoptic camera is proposed, where the BOS light field is given as $\vec{D}$, which is a vector function, as shown in Equation 6.1. The terms s and t indicate the spatial position on the microlens plane where the deflection is measured, and u and v indicate the position on the main lens aperture that corresponds to the line-of-sight of the measurement. Note here that the same 4D parameterization used in Equation 4.3 is used here as well.

$$\vec{D} = \vec{D}(u, v, s, t) \tag{6.1}$$

6.2 Generation of the BOS Light Field

Images acquired with conventional BOS typically have a large DOF which is achieved by imaging with a small aperture lens. Thus, rendered perspective views are a good starting point due to their large DOF. It is important that the experimental BOS setup takes the DOF of a rendered perspective view into consideration. Equation 6.2 shows how to calculate the effective aperture diameter, d_{eff}, used for a perspective view generation, where p_p is the

pixel pitch, s_i is the distance in image space, and f_{micro} is the focal length of a microlens. This diameter is used to calculate the DOF (Equations 5.1 and 5.2) instead the diameter of the main lens aperture, d_a, when determining how to setup a given BOS experiment using a plenoptic camera. This combination for the rest of this discussion is termed plenoptic BOS.

$$d_{eff} = \frac{p_p s_i}{f_{micro}} \tag{6.2}$$

Once raw plenoptic images are acquired with and without the presence of the flow field disturbance, both plenoptic images are processed to generate the same number of perspective views. A perspective view pair consists of two images of same rendered perspective with and without the presence of the density disturbance. This pair can be used to determine the background displacements for that particular line-of-sight. Displacement vectors from a single perspective view image pair are equivalent to conventional BOS; however with a plenoptic camera, the process can be repeated for all perspective views. This creates the ability to produce multiple BOS measurements, where each possesses a slightly different line-of-sight. The main difference between plenoptic BOS and conventional BOS at this stage is that more lines-of-sight have been observed with plenoptic BOS at a lower spatial resolution.

In this work, a 2D cross-correlation algorithm developed by Fahringer *et al.* [48] was used to determine the background displacements per perspective view image pair. This algorithm uses an iterative multi-pass, multi-grid window deformation technique known as *WIDIM* developed by Scarano *et al.* [49]. The vectors determined for each experiment used a final interrogation window size of 8×8 pixels with fifty-percent overlap. This means that a single vector represents 8×8 pixels, which is actually a representation of several microlenses in a perspective view. Interpolation of such values is performed at this stage to ensure that each pixel ("microlens") is assigned a displacement value. This interpolation step does not increase the amount of displacement information originally obtained using cross-correlation, rather this step serves as a way to return to the same resolution used to render the perspective view images. Using all of the displacement information from each of the perspective views, a

4D matrix of displacements is created to fill out the BOS light field, where each perspective view represents a fixed (u, v) value and each (s, t) represents the interpolated values assigned to each microlens from the cross-correlation results.

This process is represented in Figure 6.1, where three perspective view image pairs have been generated, and the cross-correlation algorithm has been implemented to provide a vector result of the top center portion of each image pair. This example is simplified such that the final interrogation window size represents a region of 2×2 microlenses in the overall microlens array. A zoomed-in view of the four microlenses is shown at the bottom of the figure. The single vector determined from the cross-correlation process from a perspective view image pair corresponds to the same (u, v) value, or pixel location, behind each of the four microlenses. While this schematic shows results from just three perspective view image pairs with respect to four microlenses, this concept represents the ability to generate the entire BOS light field captured for all perspective views generated from the raw images captured by a plenoptic camera.

6.3 BOS Refocusing

Just as conventional light field data is used to render a synthetic refocused image, BOS light field data is used to generate a 'focused' BOS image. This concept is represented by a new refocusing equation in Equation 6.3, where all the displacement information behind each microlens is summed for all the angles it possesses. The term α represents that same scalar value used to signify a relative depth of the synthetic film plane from Equation 4.5. In this case, the output vector is divided by the number of perspective views such that it is an average of the line-of-sight values passing through that particular point. This vector can possess a value representing the x and y components of the displacement vector individually, or can be used to determine the magnitude of the displacement vectors.

$$\vec{I}_{refocus}(s', t') = \iint \vec{D}\left(u, v, u + \frac{s' - u}{\alpha}, v + \frac{t' - v}{\alpha}\right) du\, dv \tag{6.3}$$

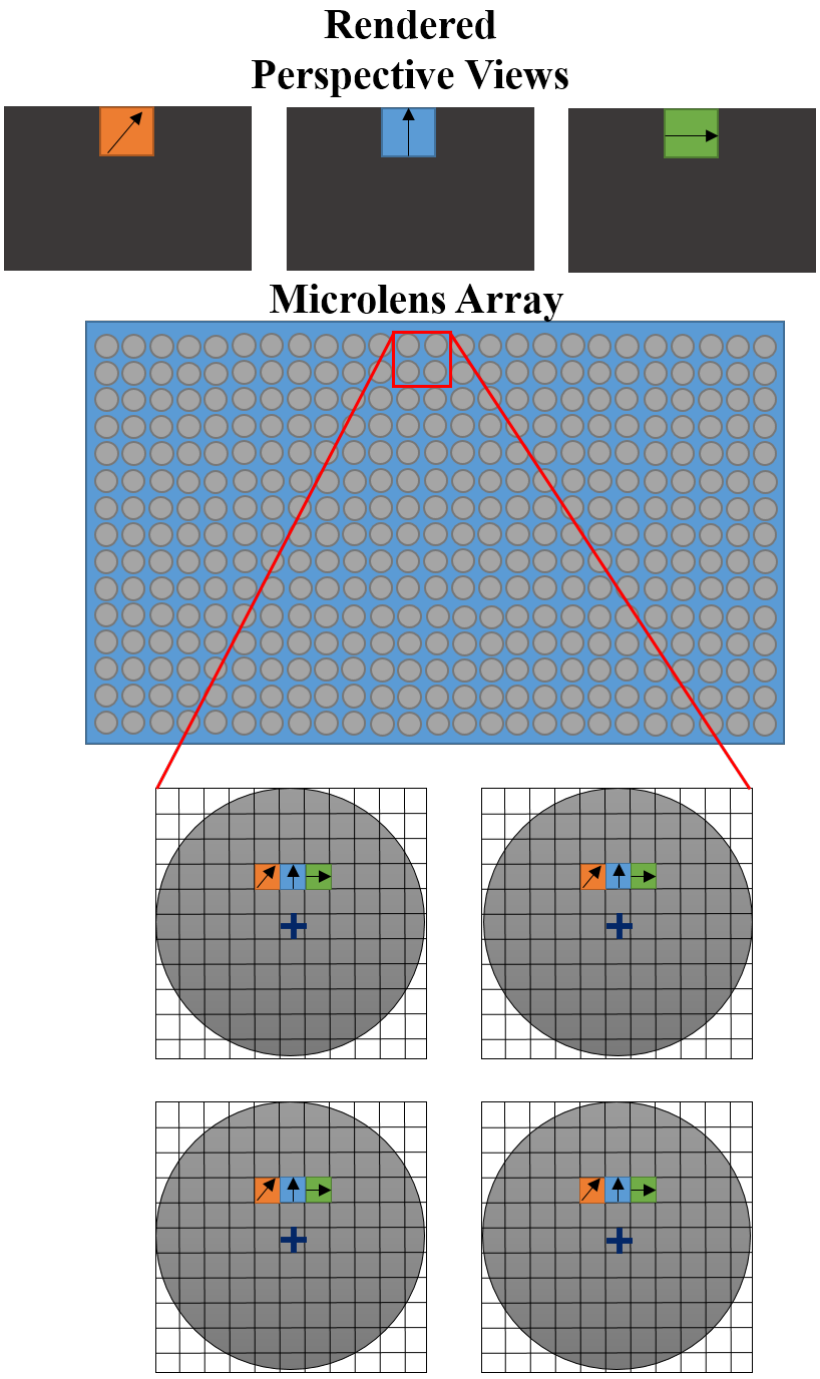

Figure 6.1: Schematic representing a simplified version of generating the BOS light field, where three perspective view image pairs are used. The vector shown in the top center portion of each perspective view represents a 2×2 region of microlenses in the array. For each of the four microlenses, the vector value for each perspective view corresponds to the same pixel location behind each microlens.

The focused BOS image will exhibit similar features as a conventional focused schlieren images. In particular, the image will have a finite DOF with features going in and out of focus as the synthetic focal plane is adjusted. The main difference between conventional focused schlieren images and BOS focused images lies in the fact the plenoptic BOS generates these focused images from just two raw plenoptic images. In order to observe gradients at different focal planes with conventional focused schlieren, the focal plane position would have to be manually shifted in order to acquire new images. Another difference is that focused BOS images are now representative of a vector field rather than the scalar field represented in both conventional schlieren imaging and focused schlieren imaging.

There is also an increased signal-to-noise ratio (SNR) with depth inferred from focus compared to that of a single perspective view image pair. A perspective view image pair has a large DOF in order to ensure that both the background and the density disturbance are in-focus. Such large DOF allows for noise to be more evident in images containing all in-focus features. With focused BOS images, the DOF is expected to be a function of the spatial resolution of the vector field measurement. This is defined as the final window size used in the cross-correlation based algorithm. Depending on the window size of the interrogation window, the consequence is that the DOF can be quite large in comparison to the refocused images rendered from original image data. Exploration of both qualitative and quantitative aspects of focused BOS images are provided in the following experimental discussions.

Chapter 7

Experimental Arrangements

Raw images from a plenoptic camera were processed using in-house codes written in both MATLAB and C on a computer with 6 cores and 16.0GB of RAM. These codes provide functions for calibration, generation of perspective views, cross-correlation of image pairs, creation of the BOS light field, and generation of BOS focal stacks. Table 7.1 shows the computational time of each step in this process. The most time is spent generating the focused BOS images. It takes approximately 43 minutes to generate 500 slices for a BOS focal stack, which is the most computationally expensive step in this process. With further development of the plenoptic BOS process, there is potential to decrease this step significantly in the future. Images were resampled and rendered with a resolution of 914×602. This does not increase the actual resolution in the image or increase the amount of real data obtained during image acquisition.

The experiments in this section used wavelet-based generated backgrounds. The backgrounds were created based off wavelet noise algorithms developed by Cook *et al.* [50]. The generated background consists of individually band limited noise functions produced at resolutions of $2^8 \times 2^8$. Multi-scale patterns in a single background provide the ability to detect distortions on a wide range of scales during data acquisition [51]. For each of the following experiments, the background was printed on large poster paper and mounted to a fixed location during image acquisition. Specific dimensions for each experiment are mentioned in their respective sections.

Step in Plenoptic BOS Process	Time
Generation of Original Light Field	14.2 seconds
Generation of All Perspective Views (for both images with and without disturbance)	9.6 seconds
Cross-Correlation Performed on a Single Perspective View Image Pair	2.6 seconds
Cross-Correlation of All Perspective View Image Pairs	9.7 minutes
Generation of BOS Light Field	1.1 seconds
Generation of 500 Focused BOS Images (saved as .mat and/or .tif images)	43.4 minutes
Generation of a Single Focused BOS image	5.4 seconds

Table 7.1: Computational time for each step in the plenoptic BOS process.

7.1 Experiment One: Two Flame Sources

The experiment discussed in this section was set up in the AFDL's experimental facility, and it was designed to qualitatively explore density gradients produced at two different known depths. Figure 7.1 shows a side view schematic of the experimental setup, where two flames are placed at different depths. The front flame was a hand held lighter with an inner diameter of 5 mm, and it was placed at 365 mm in front of the nominal focal plane. The back flame was a standard natural gas Bunsen burner with an inner diameter of 11 mm, and it was placed 177 mm behind the nominal focal plane. The distance between the two flames was 542 mm, and the overall DOF was 1246 mm. The DOF was determined by using a magnification of -0.11 and a circle of confusion on the image plane of approximately one microlens. This DOF allowed for both the schlieren objects and the background to be well within focus in rendered perspective view images. The focal length of the main lens was 135 mm, and the f# was approximately 4. The background was printed on paper that was

approximately 0.6 m×0.6 m in order to fill the desired field of view, and it was illuminated by two LED desk lights.

During the cross-correlation process, a cropping feature was implemented in order to hone in on the density distortions produced by the two flames. The cross-correlation was performed on a cropped portion of the image for two reasons: 1) to exclude areas where distortions are not present, and 2) to eliminate the area containing the flames themselves. The latter reason is due to the tip of the hand held lighter not being present in the image acquired without the presence of the flame. This creates erroneous displacements during the cross-correlation process. The luminescence of the flame would also interfere with the background, which would hinder the ability to make a successful cross-correlation. In future experiments, this can potentially be avoided through spectrally filtered illumination and collection optics. The cropped region ranged from 240 to 720 pixels in the x-direction and 60 to 420 pixels in the y-direction. A collection of 500 focused BOS slices in a focal stack were rendered upon completion of building the BOS light field. The increments between slices was 3.31 mm.

7.2 Experiment Two: A Single Heated Jet

The second experiment was performed at NASA Langley Research Center in Virginia. The background was printed on paper with the approximate dimensions of 0.9 m×0.9 m, and it was mounted to one end of a 3.7 meter long optical table. A single hot air jet was used as the Schlieren object, where the temperature of the heated jet was set to 144° Celsius. The outer diameter of the heated jet was 31.75 mm. The flow box used to produce the jet was made up of three electrically resistive finned strip heating elements. There was a circular opening in the bottom of the box, which is where room temperature air entered the heating process. As the air was heated, it became naturally buoyant and flowed out of a circular hole at the top of the flow box. Attached to the top hole was a nozzle for these experiments.

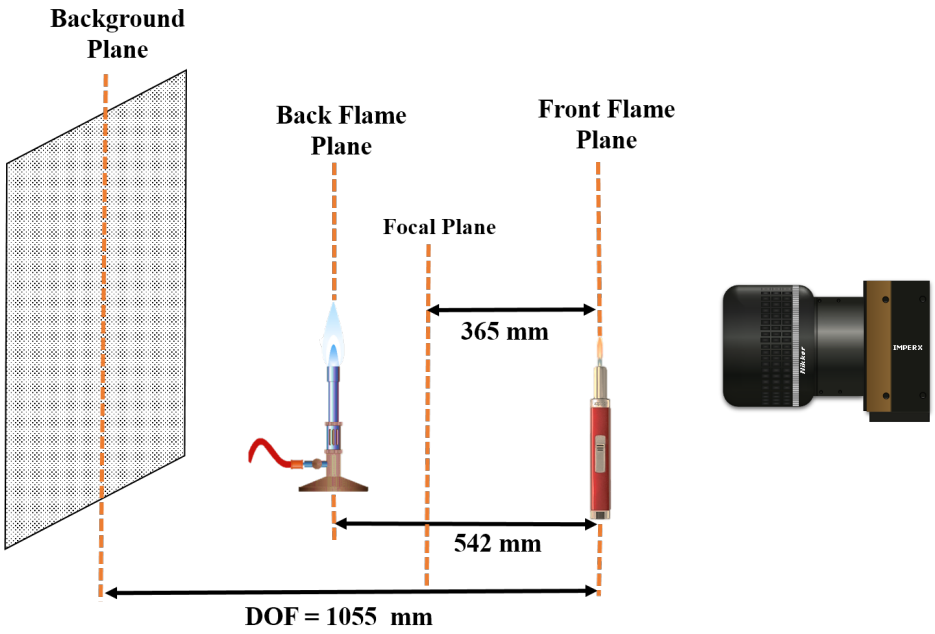

Figure 7.1: Side view schematic of the Plenoptic BOS setup observing two flames produced at different depths within the scene.

The nozzle was 152.4 mm tall, and it had a contoured shape such that the inner diameter started at 50.8 mm and ended at 25.4 mm.

Both the background and the focal plane were fixed for this experiment. The nominal focal plane was set to be approximately 635 mm in front of the background. A 135 mm main lens was used, where the approximations for the f# and the magnification were 4 and -0.05 respectively. Using these camera parameters and a circle of confusion of one microlens, the DOF for rendered perspective view images was calculated to be approximately 5.5 meters. With the constraints of the optical table being used in the lab facilities, only a portion of this DOF was actually used. The schematic in Figure 7.2 represents the area used during this experiment known as the *region of interest*. Within the region of interest, the heated jet was moved to ten positions with respect to the nominal focal plane position. These positions ranged from 304.8 mm behind the nominal focal plane to 1066.8 mm in front of the nominal focal location. There were 25 reference images acquired without the flow box turned on. At each of the ten positions, 25 images of the jet were taken. This allows for the plenoptic BOS

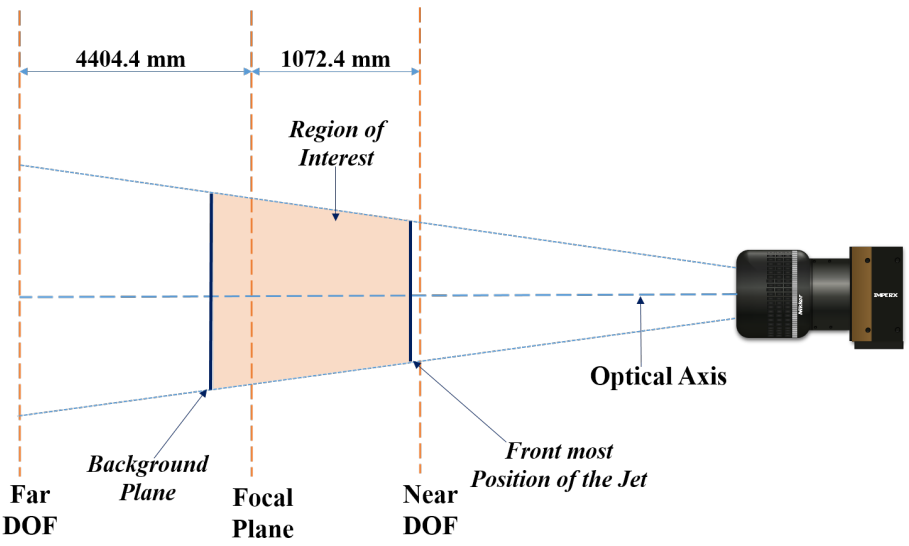

Figure 7.2: Schematic of the experimental BOS setup of a single heated jet performed at the NASA Langley Research Center. The region of interest is the portion of the DOF used during these experiments, where the heated jet was placed at ten different positions within this region.

process to be executed with respect to both instantaneous and ensemble averaged images. A cropped region was also implemented during the cross-correlation stage of this analysis. The cropped region ranged from 300 to 600 pixels in the x-direction and 100 to 350 pixels in the y-direction. A collection of 500 focused BOS slices in the focal stack were also rendered in this experiment upon completion of building the BOS light field for each heated jet position. The increment between slices was 2.04 mm.

An additional step was taken during this experiment in order to improve the BOS results. This additional step required taking a series of dot card images through the scene in the depth direction. These dot cards had square dots that were 6.35 mm with 12.7 mm spacing between them. The dot card images were taken at 6 different depth positions ranging from 254 mm behind the nominal focal plane to 1143 mm in front of the nominal focal plane. The purpose of these dot card images was to appropriately calibrate the scene. The algorithm used to implement this dot card calibration directly generates the reconstructed volume by mapping any point in object space to a point on the image sensor. Such a mapping can be determined by generating perspective views of each dot position, determining the location

of the dots for each perspective, and then using all dot locations per perspective view per depth location to solve a least-squares mapping function through the volume. This work is going to be presented at the AIAA SciTech Conference in January 2017 by Elise Hall and Timothy Fahringer.[52]

Chapter 8

Post Processing and Discussion of Results

8.1 Experiment One: Two Flame Sources

Figure 8.1 shows the magnitude of the background displacements obtained for a center perspective view. These cross-correlation vectors are overlaid on the center perspective view for visual guidance. This figure, used for purely qualitative purposes, shows the cropped region used during cross-correlation as well as the placement of the two flames within the scene.

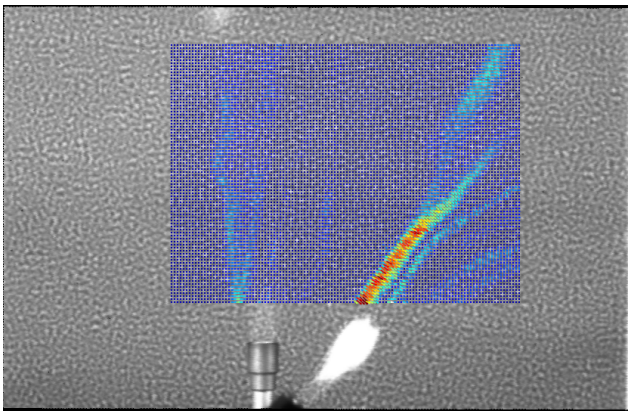

Figure 8.1: Overlaid image of the cropped region of vectors determined from cross-correlation of the center perspective image pair on top of center perspective of the two flames themselves. This provides visual guidance as to the location of the two flames within the setup.

In order to observe differences between perspective views, Figure 8.2 shows the vectors determined from a left-most perspective view image pair, a center view image pair, and a right-most perspective view image pairs respectively. There were 116×86 displacement vectors measured, where the values of the magnitude of the displacement in all three views ranged from approximately 0 to 2.6 pixels as shown in the color bar for all three sub-figures. This maximum displacement of 2.6 pixels was equivalent to approximately 0.08 mm

in physical space. Two noticeable differences can be made between these three different perspective views. The first is that the displacement values produced by the two flames are not truly identical, which shows the variation in distortion present from slightly different lines-of-sight. The second is that the shift is most apparent when looking at the displacements produced by the right flame in the top right region of each image (circled in red), where the distortions are in different positions for each of the different views. In each perspective view, the distortions created by the right flame are more visually observable than those of the left flame. Without further analysis, this could be due to the flame being closer to the camera or the presence of stronger density gradients. While it is known from the experimental setup that one flame is placed in front of the other, the depth cannot really be inferred based on these vector outputs. Further investigation would be required to do so.

The collective displacement information obtained from 225 perspective views provided the ability to generate a focal stack of focused BOS images. In actuality, information from only 121 different views were used for two reasons: (1) there was a lack of information present in perspective views generated near the edges of circular main lens projected onto each microlens and (2) the black space between each of the microlenses does not provide any information about the scene. Figure 8.3 shows examples of two synthetically generated focused BOS images. As a reminder, these images were rendered after the series of plenoptic BOS steps were implemented using the two raw plenoptic images acquired. These two focal slices correspond to the depth location in which the back flame and front flame provide the most in-focus distortions. The detail of each flame structure is apparent when it is in-focus, but blurred when it is out-of-focus. This is most readily observed by the left flame, where the wrinkling in the density gradients in the vertical direction are more apparent when the left flame is in-focus (8.3b). These same type of wrinkling details are not apparent in the right flame until the synthetic focal plane is adjusted to the forward location (Figure 8.3a). The synthetic focal planes that correspond to each of these focused BOS images signifies

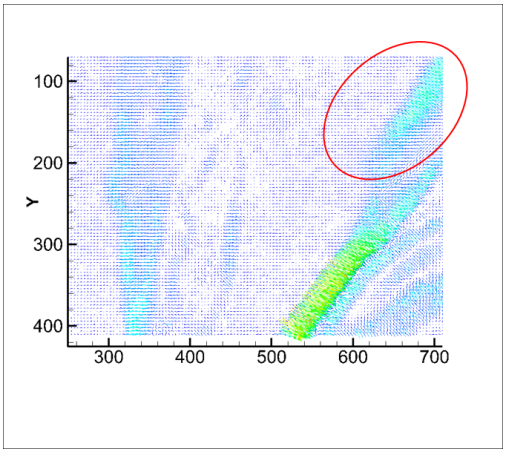

(a) Leftmost Perspective View

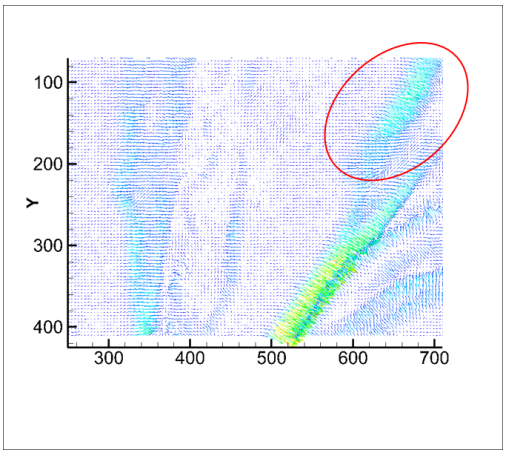

(b) Center Perspective View

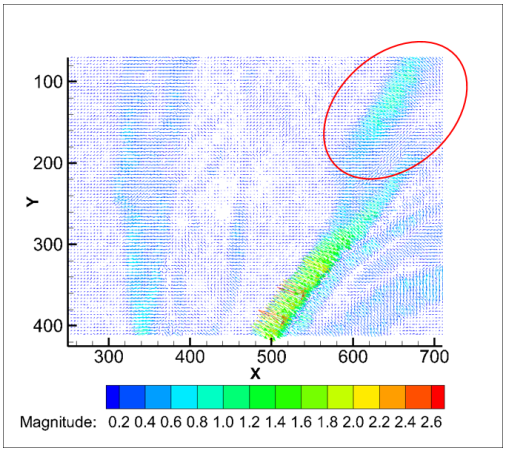

(c) Rightmost Perspective View

Figure 8.2: Examples of the magnitude of the displacement vectors obtained from the cross-correlation of three different perspectives view image pairs. Each sub-image contains 116×86 displacement vectors.

that the left flame is behind the right flame. Qualitative observations such as these provide the ability to infer depth from focused BOS images.

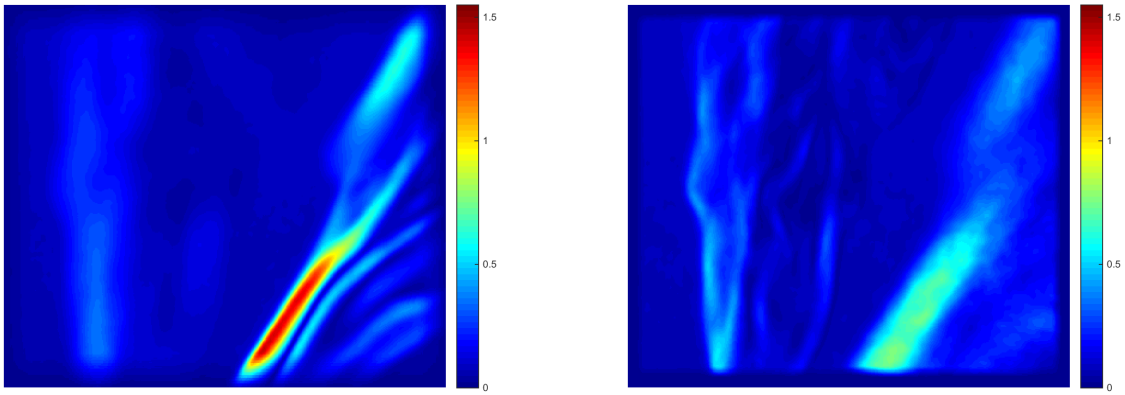

(a) (b)

Figure 8.3: Refocused BOS images where the magnitude of the distortions of the front and back flame are in-focus at different depth positions.

It is also interesting to note that the focused BOS images seem to show more, or at least more easily discerned, detail than the corresponding 'all in focus' perspective view images. This is due to the fact that each focused BOS image is a combination of all the perspective view images, effectively increasing the SNR. The narrow DOF also causes features not contained at a particular depth to become blurred, thus providing better distinction of features contained at different depths. A side by side comparison of this observation is shown in Figure 8.4.

It is important to note at this stage that both x and y displacement values can be used separately to generate focused BOS images. This allows for displacement occurring in either direction to explored individually. Figures 8.5 and 8.6 show examples of focused BOS images generated from x and y displacements separately. In this experiment, it was observed that the x displacements played the most significant role in the generation of the magnitude of the displacements. By exploring displacements in a single direction, the strength of a focused BOS image can be observed. For instance, in looking at just the y displacements in Figure

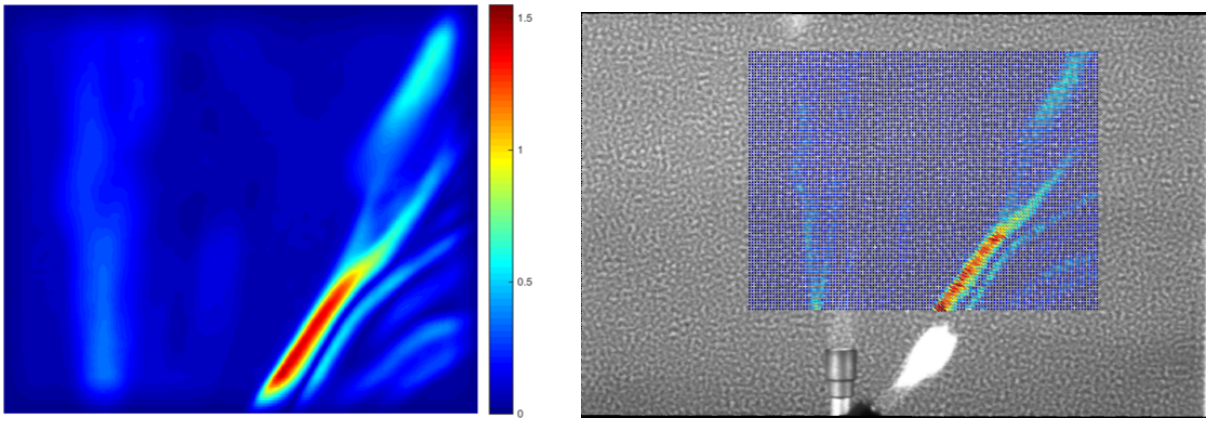

(a) (b)

Figure 8.4: Comparison of the results produced by a single focused BOS image and a single perspective view cross-correlation.

8.6, the detail of the back jet is almost unobservable when the focal plane is located at the front flame's position. This is similar to that of the focused schlieren experiment discussed in Chapter II, where disturbances occurring at locations other than the focal plane appear blurred and unclear.

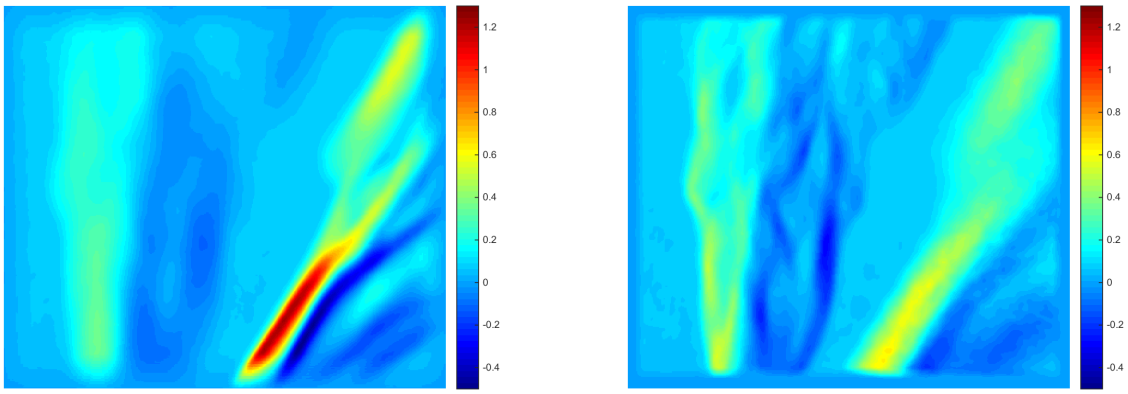

(a) (b)

Figure 8.5: Refocused BOS images where the x-displacement of the distortions of the front and back flame are in-focus at different depth positions.

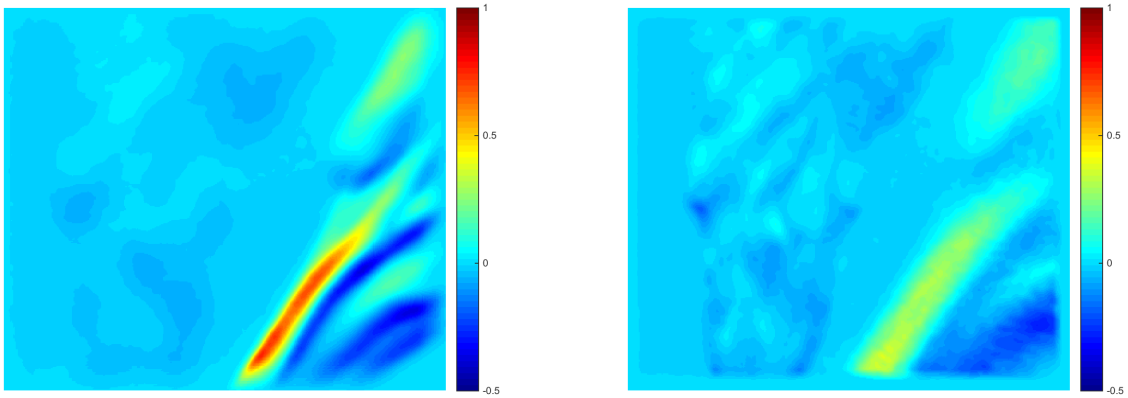

(a) (b)

Figure 8.6: Refocused BOS images where the y-displacement of the distortions of the front and back flame are in-focus at different depth positions.

8.2 Experiment Two: A Single Heated Jet

During this experiment, 25 images were acquired at each of the ten positions of the heated jet. Acquiring 25 images allowed for observation of both ensemble averaged and instantaneous flow fields. An example of the difference between these two results is shown in Figure 8.7, where the heated jet in this case was placed at 762 mm in front of the nominal focal plane. The average result has the ability to eliminate any turbulent fluctuations or room air movement that might have been present in just a single frame. In both of these sub-figures, the number of displacement vectors was 71×58, and the maximum magnitude of the distortion was approximately 0.55 pixels, which is equivalent to 0.9 mm in physical space.

This data was also used to preliminarily estimate the depth corresponding to the heated jet position. The average images were used to make these estimations, and an assumption was made that the jet was considered a flat object positioned at a single depth within the focused BOS image volume. The 500 focused BOS image slices were used during this depth estimation. Using a MATLAB code, the gradients of each of the 500 slices for each heated jet position were determined. The 100 maximum gradient values per slice were averaged to

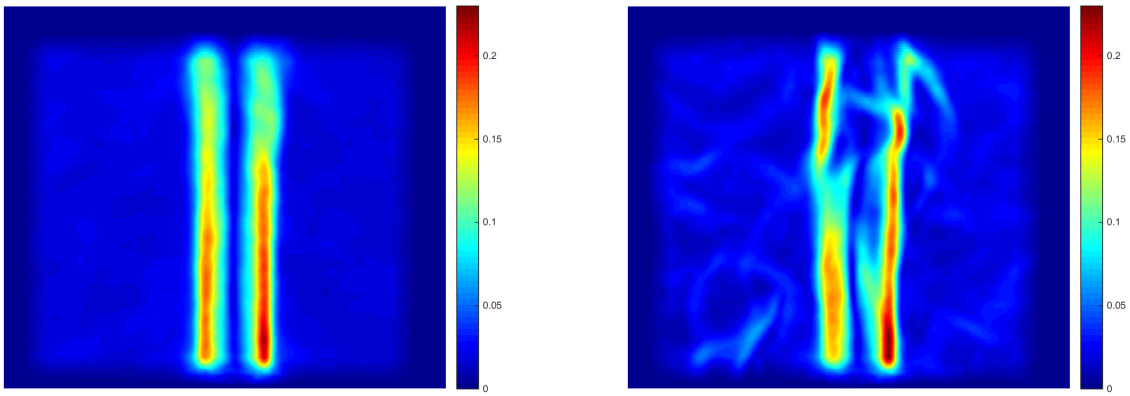

(a) Average focused BOS Image

(b) Instantaneous focused BOS Image

Figure 8.7: Results of plenoptic BOS using an average of the 25 heated jet images versus using an instantaneous heated jet image. Both images have been rendered for the focal plane position corresponding to their depth position of 762 mm in front of the nominal focal plane.

obtain a single gradient value representative of each of the 500 slices. The largest gradient value within the stack of 500 slices corresponded to the plane at which the jet was most in-focus, therefore the plane that corresponded to the jet's position. For each of the ten positions, the actual and estimated depth locations are shown in Figure 8.8. Both the estimated and actual positions of the jet were measured in millimeters with respect to the camera's position. For reference, the line $y = x$ is plotted alongside the results. The near and far DOF limits are also shown in this plot to show the region defined as in-focus for each given object position. This DOF was calculated by using the smallest interrogation window size and the specified position in object space of each jet location. Error bars have also been placed in the horizontal direction at each jet position, which represents the width of the jet itself. Although the assumption was made that the density gradients occur at a single plane, this error bar provides the ability to observe the finite width associated with this estimation. The largest error from this plot occurs at the location in which the jet was placed farthest from the camera and closest to the background. This resulted in approximately a 7% error, which equates to a 238 mm difference between the actual and estimated depth location.

While preliminary in nature, this simple depth estimation algorithm shows the ability to estimate the position of density gradient production in 3D space.

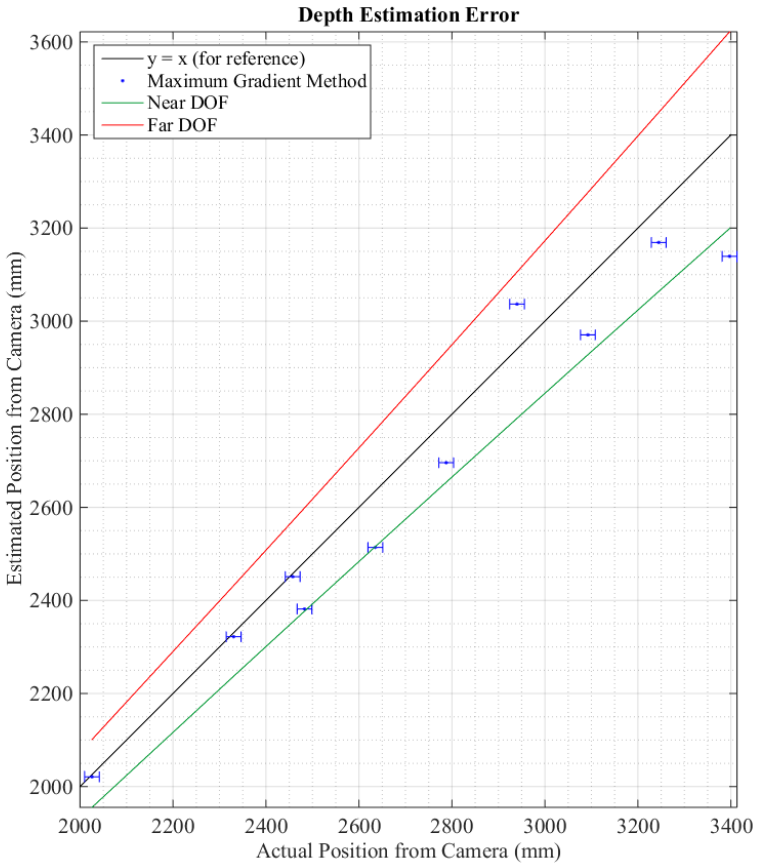

Figure 8.8: Error of the depth estimation method versus the actual position of the jet measured with respect to the distance away from camera in terms of millimeters. The near and far DOF limits are also shown for each jet position, and a horizontal error bar represents the finite width of the jet being imaged.

With regards to earlier discussions about DOF, a BOS setup is considered most sensitive when the schlieren object is placed at the position s_{near}. This means that the observable displacements of the background in the BOS setup will decrease as the schlieren object gets closer to the background. Using the theoretical geometric relationship in Equation 2.6 with respect to this data set, a direct relationship was observed between the magnitude of the displacement and the distance between the schlieren object plane and the background. As

the distance between the two planes decreased, the measurable displacement also decreased. The heated jet position closest to the background versus furthest from the background was determined to have an order of magnitude less in measured displacement values.

Figure 8.9 shows each of the ten jet positions and the maximum gradient values determined for each slice in their respective 500 slice focal stack. The sensitivity of the BOS measurements in this experiment are also observable with respect to the maximum gradient values used for the depth estimation process. This plot shows several key points: (1) the observable peak, or the maximum value, of the gradients is more distinguishable at jet positions closer to the camera, (2) the values of the maximum gradients decreased by an order of magnitude between the closest jet position and the farthest jet position, and (3) as the peak became less observable, there was a decrease in the ability to accurately estimate the depth of the jet position. With the order of magnitude difference between the front most jet position and the back most jet positions, it is really difficult to discern the peak of the back most position. When these two positions are plotted separately, these is an observable peak for the back most position. A side by side comparison of the maximum gradient values representing each slice for both the back most and front most positions of the jet are shown in Figure 8.10. Such results are not apparent when using the same scale to plot all positions. It can also be noted that the sensitivity of this system would change if the background position were places further away. The full DOF was not utilized in this setup due to laboratory constraints. If the background were positioned further back in the DOF region, the back most position of the jet in this experiment would increase in sensitivity. The relationship between the density gradient produced at a certain position in the scene relative to the background position highly supports the known sensitivity of a BOS setup.

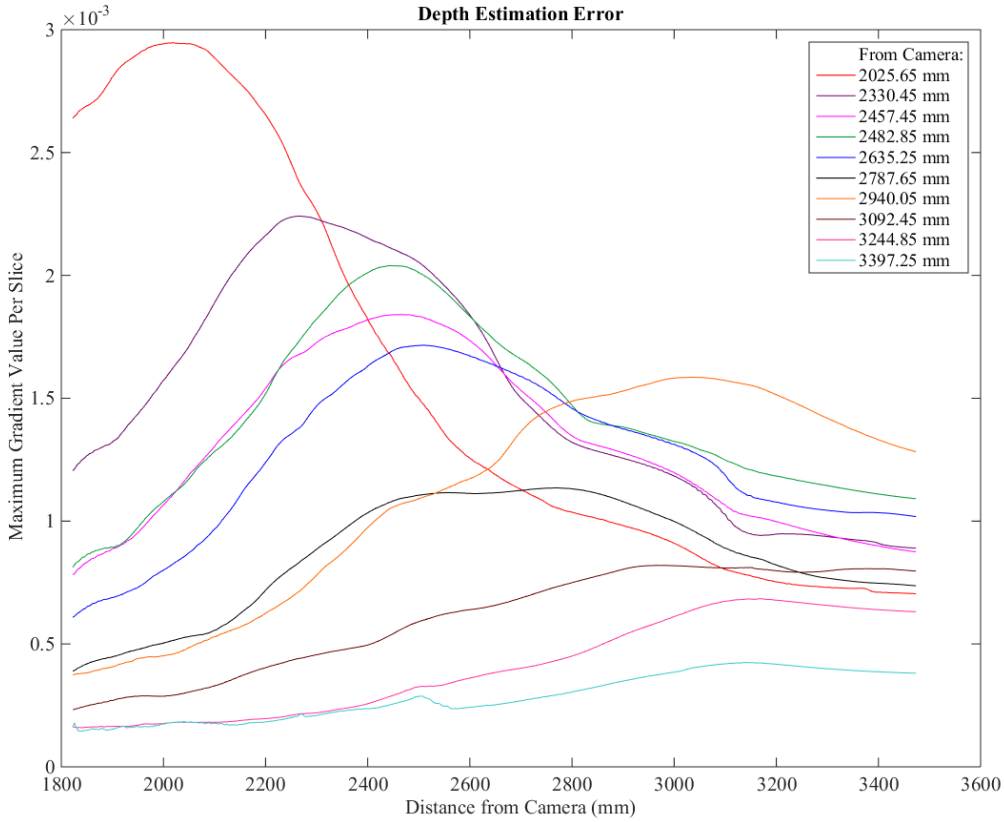

Figure 8.9: Maximum gradient values per slice of each of the 500 slices in the focal stack of focused BOS images generated for each of the ten different jet positions. The maximum gradients are plotted with respect to the distance from the camera in millimeters.

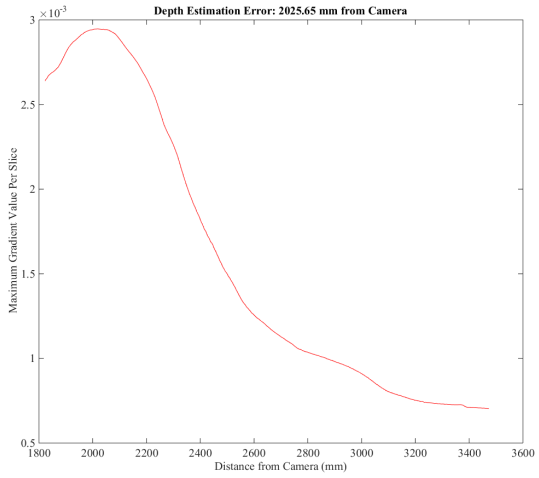

(a)

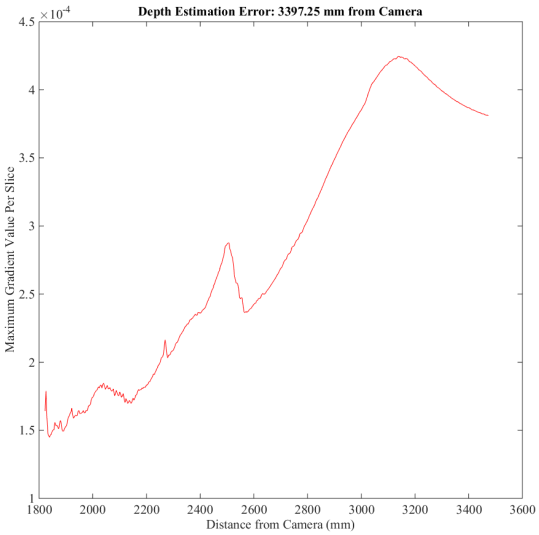

(b)

Figure 8.10: Maximum gradient values per slice of each of the 500 slices in the focal stack of focused BOS images generated for (a) the front most jet position and (b) the back most jet position.

Chapter 9

Conclusions and Future Work

This work presents the results of a plenoptic camera with the background oriented Schlieren technique. This simple schlieren technique exploits the refractive index changes due to the presence of an inhomogeneous density field. The plenoptic camera provides the ability to capture spatial and angular information in a single snapshot, which can be computationally refocused or shifted in perspective in the post-processing period. Incorporating these features into the BOS technique provides the opportunity to explore three-dimensional qualities of a density-varying flow field.

During a plenoptic BOS experiment, it is important to consider the appropriate experimental setup based on the imaging system. The depth of field for plenoptic BOS is based on parameters used to generate a single perspective view. By doing so, this will allow both the background and schlieren object to be in-focus during the generation of all perspective view image pairs. During the post-processing of an experiment, an image comparison algorithm such as a 2D cross-correlation algorithm is used to obtain displacements between these pairs. All of the displacement is then able to be combined in order to generate focused BOS images, which provides a way to qualitatively infer depth of the schlieren object location. It is also possible to quantify such depth position of the schlieren object by using a gradient-based depth estimation algorithm.

Two preliminary experiments investigated the plenoptic BOS process. The first experiment used two flames places at different locations in the scene. Upon completing the plenoptic BOS process, focused BOS images provided the ability to infer depth about the positions of both flames. These results also showed comparable results to that of focused schlieren but in a much simpler manner. The success of this experiment provides motivation

for this new approach to be implemented in applications where disturbance locations might be unknown beforehand.

Also, images were acquired of a single heated jet placed at ten different locations with respect to the fixed focal plane position. This experiment showed another success in providing qualitative focused BOS images, but it also provided preliminary depth estimation calculations for each of the ten positions. These depth estimations were calculated by taking the gradient of each slice in a 500 focused BOS image focal stack and determining the location corresponding to the maximum gradient value. While preliminary in nature, these results demonstrate the ability to quantify the position of the heated jet in 3D space. These results also supported the well-known concept of sensitivity in a BOS setup, where the jet positioned furthest from the background produced the most accurate depth estimation values. As the jet position moved closer to the background, the error depth estimation increased. The highest error was 7%, which corresponded to 238 mm in physical space.

These two experiments have provided proof that the plenoptic BOS technique can produce 3D, qualitative results. The results also provide preliminary success in estimating the depth at which such density distortions occur within a given setup. There is motivation to continue the implementation of plenoptic BOS in density-varying flow experiments, especially in laboratory facilities possessing limited optical access. The development of this new technique also provides motivation to continue the development of this technique particularly with respect to advancing towards the ability to reconstruct a 3D density field.

There are several items that will be explored in the future in order to advance the plenoptic BOS technique. First, a comparison between measurements obtained with a conventional BOS system and a plenoptic BOS system will be made. This will provide the ability to discern when each method might be favorable as well as what limitations need to be considered for each type of system. Additional work will also explore additional algorithms that can be implemented to improve the quality of BOS results. Such algorithms include the potential use of optical flow algorithms instead of a cross-correlation based method. Optical flow [51]

has been used in conventional BOS systems, which provides reason to explore them with regards to plenoptic BOS as well. Another algorithm to explore is the use of a deconvolution algorithm during image processing. Such work has already been performed with regards to plenoptic imaging [53], but incorporating such work into BOS measurements has not been done yet. The implementation of this algorithm would provide the ability filter out information that is not considered in-focus at a specified synthetic focal plane. This would be highly favorable for problems where there are overlapping disturbances in the field-of-view.

Additional work also includes the transition of this technique to both 3D and quantitative measurements. This major leap will not be performed all at once. This will consist of a series of steps that will require advanced knowledge of the plenoptic camera, the ability to simulate a plenoptic BOS setup using a single (or multiple) plenoptic camera(s), and also taking time to review of the fundamentals of tomography. Tomography is a complex problem that has been used to reconstruct 3D density fields from data acquired by 3D BOS systems, but incorporation of this algorithm into plenoptic BOS measurements will be a major step in advancing this technique. Such work is motivated by simplifying the data acquisition and reconstruction process compared to the systems typically used today.

Bibliography

[1] AirTeamImages. F/A-18A Hornet, 2009.

[2] Daniel Floryan, Jerrod Hofferth, and William Saric. Design , Assembly , and Calibration of a Focusing Schlieren System. pages 1–11, 2012.

[3] J. M. Cabaleiro, J. L. Aider, G. Artana, and J. E. Wesfreid. Single camera time-resolved 3D tomographic reconstruction of a pulsed gas jet. *Journal of Visualization*, 16(4):263–274, 2013.

[4] Bradley Atcheson, Ivo Ihrke, Wolfgang Heidrich, Art Tevs, Derek Bradley, Marcus Magnor, and Hans-Peter Seidel. Time-resolved 3d capture of non-stationary gas flows. *ACM Transactions on Graphics*, 27:1, 2008.

[5] Erik Goldhahn and Jörg Seume. The background oriented schlieren technique: Sensitivity, accuracy, resolution and application to a three-dimensional density field. *Experiments in Fluids*, 43:241–249, 2007.

[6] Masanori Ota, Kenta Hamada, Hiroko Kato, and Kazuo Maeno. Computed-tomographic density measurement of supersonic flow field by colored-grid background oriented schlieren (CGBOS) technique. *Measurement Science and Technology*, 22(10):104011, 2011.

[7] F. Nicolas, V. Todoroff, A. Plyer, G. Le Besnerais, D. Donjat, F. Micheli, F. Champagnat, P. Cornic, and Y. Le Sant. A direct approach for instantaneous 3D density field reconstruction from background-oriented schlieren (BOS) measurements. *Experiments in Fluids*, 57(1):1–21, 2016.

[8] Gordon Wetzstein, Ramesh Raskar, and Wolfgang Heidrich. Hand-Held Schlieren Photography with Light Field Probes. *Iccp*, pages 1–8, 2011.

[9] Abhishek Bichal. *Development of 3D Background Oriented Schlieren with a Plenoptic Camera*. PhD thesis, Auburn University, 2015.

[10] Marc Levoy. Light Fields and Computational Imaging. *IEEE Computer Society*, pages 46–55, 2006.

[11] Ren Ng, Marc Levoy, Mathieu Brédif, Gene Duval, Mark Horowitz, and Pat Hanrahan. Light Field Photography with a Hand-Held Plenoptic Camera. pages 1–11, 2005.

[12] Gary S. Settles. Basic Concepts. In *Schlieren and Shadowgraph Techniques*, pages 25–28. Springer-Verlag, 2001.

[13] G. S. Settles. *Schlieren and Shadowgraph Techniques*. Springer-Verlag, New York, 2001.

[14] Amrita Mazumdar. Principles and Techniques of Schlieren Imaging. pages 1–16, 2011.

[15] G.E.A. Meier. Hintergrund Schlierenmessvefahren. *Deutsche Patentanmeldung*, (DE 199 42 856 A1), 1999.

[16] M Raffel, H Richard, and G E A Meier. On the applicability of background oriented optical tomography for large scale aerodynamic investigations. *Experiments in Fluids*, 28(5):477–481, 2000.

[17] J. S. Goulding. A Study of Large-Scale Focusing Schlieren Systems. 2006.

[18] Bradley Atcheson, Ivo Ihrke, Wolfgang Heidrich, Art Tevs, Derek Bradley, Marcus Magnor, and Hans-Peter Seidel. Time-resolved 3d capture of non-stationary gas flows. *ACM Transactions on Graphics*, 27(5):1, 2008.

[19] François Nicolas, Francis Micheli, David Donjat, Aurélien Plyer, Fréderic Champagnat, and Guy Le Besnerais. 3D reconstruction of compressible flow by synchronized multi camera BOS. 2016.

[20] M Ota, H Kato, and K Maeno. Improvements of Spacial Resolution of Corlored-Grid Background Oriented Schlieren (CGBOS) Technique By Introducing Telecentric Optical System and Reconstruction of Density Field. pages 1–10, 2012.

[21] Eh Adelson and Jr Bergen. The plenoptic function and the elements of early vision. *Computational Models of Visual Processing*, pages 3–20, 1991.

[22] Edward H. Adelson and John Y a Wang. Single lens stereo with a plenoptic camera. *IEEE Transactions on Pattern Analysis and Machine Intelligence*, 14(2):99–106, 1992.

[23] Ren Ng. *Digital Light Field Photography*. PhD thesis, 2006.

[24] R. Hooke. *Micographia*. J. Martyn & J. Allestry, London, 1665.

[25] LiveJournal. Schlieren Photography, 2008.

[26] E. Churchill. Schlieren, 2010.

[27] T. Kinsman. Schlieren Image Of Hot Coffee Cup, 2013.

[28] A. Phukan. Optical Techniques (Qualitative and Quantitative Flow Visualization).

[29] G.E.A. Meier. Computerized Background-Oriented Schlieren. *Experiments in Fluids*, 33, 2002.

[30] A. Bichal and B. Thurow. Development of a Background Oriented Schlieren Based Wavefront Sensor for Aero-Optics. *AIAA*, 2010.

[31] H Richard and M Raffel. Principle and applications of the background oriented schlieren (BOS) method. *Measurement Science and Technology*, 12(9):1576–1585, 2001.

[32] H. Richard, M. Raffel, J. Kompenhans, and G. E. A. Meier. Demonstration of the applicability of a Background Oriented Schlieren (BOS) method. 2004.

[33] F Klinge, M Hecklau, M Raffel, J Kompenhans, and U Göhmann. Measurement of the position of rotor blade vortices generated by a helicopter in free flight by means of stereoscopic Background Oriented Schlieren Method (BOS). *Proc. 13th Intl. Symp. on Applications of Laser Techniques to Fluid Mechanics*, pages 1–12, 2006.

[34] Michael J Hargather and Gary S Settles. Background-oriented schlieren visualization of heating and ventilation flows: HVAC-BOS. *Hvac&R Research*, 17(5):771–780, 2011.

[35] Michael John Hargather and Gary S. Settles. Natural-background-oriented schlieren imaging. *Experiments in Fluids*, 48:59–68, 2010.

[36] Brett F. Bathel, Stephen Borg, Stephen Jones, Austin Overmeyer, Eric Walker, William Goad, Michelle Clem, Edward T. Schairer, and Toshiharu Mizukaki. Development of Background-Oriented Schlieren for NASA Langley Research Center Ground Test Facilities. *53rd AIAA Aerospace Sciences Meeting*, pages 1–15, 2015.

[37] R. J. Adrian. Twenty years of particle image velocimetry. *Experiments in Fluids*, 39:159–169, 2005.

[38] DLR. DLR researchers first to make causes of helicopter noise visible, 2014.

[39] Friedrich Leopold, Masanori Ota, Daniel Klatt, and Kazuo Maeno. Reconstruction of the Unsteady Supersonic Flow around a Spike Using the Colored Background Oriented Schlieren Technique. *Journal of Flow Control, Measurement & Visualization*, 01(02):69–76, 2013.

[40] A. Meier and T. Roesgen. Speckle-based Background Oriented Schlieren, 2013.

[41] NASA. Ground-Based Schlieren Technique Looks to the Sun and Moon, 2015.

[42] Y Le Sant, V Todoroff, G Le Besnerais, F Micheli, Y Le Sant, V Todoroff, G Le Besnerais, and F Micheli. Multi-camera calibration for 3DBOS. 2014.

[43] A. Gershun. The Light Field. *Translated by P.Moon and G. Timoshenkoin Journal of Mathematics and Physics*, XVIII:51–151, 1936.

[44] Marc Levoy and Pat Hanrahan. Light field rendering. *Proceedings of the 23rd annual conference on Computer graphics and interactive techniques - SIGGRAPH '96*, pages 31–42, 1996.

[45] G. Lippman. Epreuves revesibles donnant la Sensation du relief. *J. Phys*, 7:821–825, 1908.

[46] Jeffrey Bolan, Elise Hall, Chris Clifford, and Brian Thurow. Light-Field Imaging Toolkit. *SoftwareX*, 2016.

[47] R. Kingslake. Depth of Field. In *Optics in Photography*, pages 84–88. 1992.

[48] Timothy W Fahringer, Kyle P Lynch, and Brian S Thurow. Volumetric particle image velocimetry with a single plenoptic camera. *Measurement Science and Technology*, 26(11):115201, 2015.

[49] F. Scarano and M. L. Riethmuller. Advances in iterative multigrid PIV image processing. *Experiments in Fluids*, 29(7):S051–S060, 2000.

[50] Robert L. Cook and Tony DeRose. Wavelet noise. *ACM Transactions on Graphics*, 24(212):803, 2005.

[51] Bradley Atcheson, Wolfgang Heidrich, and Ivo Ihrke. An evaluation of optical flow algorithms for background oriented schlieren imaging. *Experiments in Fluids*, 46:467–476, 2009.

[52] Elise M Hall, Timothy W Fahringer, and Brian S Thurow. Volumetric Calibration of a Plenoptic Camera. In *AIAA SciTech*. Auburn Univeristy (In Progress), 2017.

[53] Jeffrey Bolan. Enhancing Image Resolvability in Obscured Environments Using 3D Deconvolution and a Plenoptic Camera. 2015.